Atmospheric chemistry in East Asia determines the iron solubility of aerosol particles supplied to the North Pacific Ocean

Kohei Sakata[1,a*], Shotaro Takano[2], Atsushi Matsuki[3], Yasuo Takeichi[4], Hiroshi Tanimoto[1,5], Aya Sakaguchi[6], Minako Kurisu[7,b], and Yoshio Takahashi[8,9]

[1]Earth System Division, National Institute for Environmental Studies, 16-2 Onogawa, Tsukuba, Ibaraki 305-8506, Japan.

[2]Institute for Chemical Research, Kyoto University, Kyoto 611-0011, Japan.

[3]Institute of Nature and Environmental Technology, Kanazawa University, Kakuma, Kanazawa, Ishikawa 920-1192, Japan.

[4]Department of Applied Physics, Graduate School of Engineering, Osaka University, 2-1 Yamadaoka, Suita, Osaka 565-0871, Japan.

[5]Graduate School of Environmental Studies, Nagoya University, Furo-cho, Chikusa-ku, Nagoya 464-8601, Japan

[6]Institute of Pure and Applied Sciences, University of Tsukuba, 1-1-1 Tennodai, Tsukuba, Ibaraki 305-8577, Japan.

[7]Submarine Resources Research Center, Japan Agency for Marine-Earth Science and Technology (JAMSTEC), 2-15, Natsushima-cho, Yokosuka, Kanagawa, 237-0061, Japan.

[8]Graduate School of Science, The University of Tokyo, 7-3-1, Hongo, Bunkyo-ku, Tokyo 113-0033, Japan.

[9]Institute of Materials Structure Science, High-Energy Accelerator Research Organization Tsukuba, Ibaraki 305-0801, Japan.

[a]now at: Institute of Pure and Applied Sciences, University of Tsukuba, 1-1-1 Tennodai, Tsukuba, Ibaraki 305-8577, Japan.

[b]now at: Atmosphere and Ocean Research Institute, The University of Tokyo, 5-1-5, Kashiwanoha, Kashiwa, Chiba 277-8564, Japan.

*Corresponding author: Kohei Sakata.

Email: kohei.sakata.33@outlook.jp

ORCID: 0000-0002-0103-9631

Abstract.

The deposition of dissolve iron (d-Fe) from East Asian aerosols to the North Pacific Ocean modulates primary productivity in surface seawaters, facilitating the uptake of atmospheric carbon dioxide by the ocean, thereby affecting the global climate. Given that microorganisms in surface seawater utilize d-Fe as a micronutrient, the bioavailability of aerosol Fe depends on its fractional solubility (Fe_{sol}%). Although emission sources and atmospheric processing influence $Fe_{sol\%}$, their effects on Fe_{sol}% are incompletely understood. We assessed the factors controlling Fe_{sol}% in size-fractionated aerosol particles collected along the coast of the Sea of Japan over one year (July 2019–June 2020). Approximately 70% of d-Fe in East Asian aerosols was present in fine aerosol particles (<1.3 μm), with Fe_{sol}% ranging from 4.1% to 94.9%. Anthro-Fe accounted for approximately 50% of d-Fe in fine aerosol particles during pre- and post-lockdown of COVID-19, but its contribution was negligible during the COVID-19 lockdown period. Fe_{sol}% in fine aerosol particles was correlated with the abundance of water-soluble Fe species (Fe-sulfates and Fe-oxalate). These water-soluble Fe species were detected in mineral dust and anthropogenic aerosols in fine aerosol particles. Dissolution models optimized for Fe in mineral dust and anthropogenic aerosols demonstrated that Fe in both aerosols dissolved through proton-promoted dissolution under acidic conditions (pH < 2.0). Subsequently, d-Fe dissolved from aerosols was stabilized by the formation of Fe(III)-oxalate in the aqueous phase. Therefore, a comprehensive understanding of the chemical alteration processes of East Asian aerosols is essential for accurately quantifying their Fe_{sol}% upon transport to the North Pacific.

1. Introduction

Primary production in high nutrient–low chlorophyll (HNLC) regions is limited by the depletion of dissolved Fe (d-Fe, Martin et al., 1994; Jickells et al., 2005; Boyd et al., 2007). Ocean Fe fertilization can modulate primary production in the euphotic zone, thereby increasing the uptake of carbon dioxide and potentially exerting a remarkable influence on the global climate system (Martin, 1990; Martin et al., 1994; Falkowski et al., 2000; Jickells et al., 2005; Boyd et al., 2007). The atmospheric deposition of aerosol Fe is a dominant source of d-Fe in surface seawater in the North Pacific. Given that microorganisms in surface seawater utilize d-Fe as a nutrient (Moore et al., 2013), the bioavailability of aerosol Fe is highly dependent on fractional Fe solubility (Fe_{sol}%), which is calculated as Fe_{sol}% = (d-Fe/total Fe) × 100 (Sholkovitz et al., 2012; Mahowald et al., 2018). Although the Fe_{sol}% of aerosol particles varies considerably (0.1%–90%), the factors controlling Fe_{sol}% remain incompletely understood (Sholkovitz et al., 2012; Mahowald et al., 2018).

The difference between the Fe_{sol}% of Fe in mineral dust and anthropogenic aerosols emitted through high-temperature combustion is a potential factor controlling Fe_{sol}% in aerosol particles (Sholkovitz et al., 2012; Mahowald et al., 2018; Ito et al., 2021). Although the annual emission of anthropogenic Fe (anthro-Fe) is approximately an order of magnitude smaller than that of mineral dust Fe (mineral-Fe), anthro-Fe is a possible source of d-Fe in surface water because it exhibits higher Fe_{sol}% (up to 80%) than mineral-Fe (Fe_{sol}% < 1%; Myriokefalitakis et al., 2018; Hamilton et al., 2019; Ito et al., 2021). Indeed, the high Fe_{sol}% associated with anthro-Fe has been observed in East Asian aerosols, especially in the fine aerosol particles that they contain (Kurisu et al., 2016, 2021, 2024; L. Liu et al., 2022; Hsieh et al., 2022; Sakata et al., 2023). However, the contribution of anthro-Fe to d-Fe in aerosol particles has been poorly evaluated quantitatively through field observations. Furthermore, during atmospheric transport, mineral-Fe and anthro-Fe undergo atmospheric processes, including proton-promoted, ligand-promoted, and photoreductive dissolutions, that elevate their Fe_{sol}% (Journet et al., 2008; Shi et al., 2011a, 2015; Paris et al., 2011; Chen and Grassian, 2013; Ito and Shi, 2016; Li et al., 2017; Sakata et al., 2022). Single-particle analyses have shown that mineral-Fe and anthro-Fe in fine aerosol particles are internally mixed with sulfate, nitrate, and organic matter, including oxalate (Li et al., 2017; Sakata et al., 2022; Zhang et al., 2019; Zhou et al., 2020; Y. Zhu et al., 2020, 2022; Xu et al., 2023; Ueda et al., 2023). These internally mixed particles provide evidence of the chemical alteration of Fe-containing aerosols in the atmosphere; however, determining Fe_{sol}% through single-particle analysis remains a challenging task (Ueda et al., 2023). Therefore, the net effect of the atmospheric processes of Fe-containing particles mixed with acidic species and organic matter on Fe_{sol}% remains poorly understood.

East Asia is one of the world's largest sources of mineral-Fe and anthro-Fe transported to the North Pacific Ocean, an HNLC region (Myriokefalitakis et al., 2018; Hamilton et al., 2019; Ito et al., 2021). Additionally, East Asia continues to grapple with air pollution problems, and anthropogenic sulfate and other pollutants have been reported to cause the chemical alteration of mineral-Fe and anthro-Fe in the atmosphere over urban areas in East Asia (Li et al., 2017: Y. Zhu et al., 2020, 2022; Xu et al., 2023). Given that the Fe_{sol}% of aerosol particles supplied to the North Pacific is mainly controlled by processes occurring during transport between East Asia and Japan (Buck et al., 2013; Sakata et al., 2022), long-term observations in Japan, which is located on the eastern edge of East Asia, are crucial for providing insights into these controlling factors.

Therefore, in this study, we performed monthly collections of seven size-fractionated aerosol particles at the Noto Ground-based Research Observatory (NOTOGRO) along the coast of the Sea of Japan from July 2019 to June 2020. NOTOGRO is a suitable location for collecting long-range-transported aerosols that are minimally influenced by local emissions (Fig. 1, Sakata et al., 2021). In this study, the sampling period encompassed the COVID-19 lockdown period in China (from the end of January 2020 to February 2020) when the anthro-Fe concentration in China considerably decreased (Liu et al., 2021; Li et al., 2021; Zheng et al., 2020; Xu et al., 2022). The considerable reduction in anthro-Fe concentration due to the COVID-19 lockdown provides opportunities to assess the effect of anthropogenic activities on Fe_{sol}% in aerosol particles in East Asia. We conducted various analyses related to estimating Fe sources and alteration processes to understand the factors controlling Fe_{sol}% in the East Asia region. Atmospheric concentrations of total and dissolved metals were determined through high-resolution inductively coupled plasma mass spectrometry (HR-ICP-MS). The contributions of mineral-Fe and anthro-Fe to d-Fe were estimated on the basis of (i) positive matrix factorization (PMF, Norris et al., 2014) and (ii) the molar ratio of d-Fe relative to that of dissolved Al ([d-Fe]/[d-Al]) as a new indicator for the sources and dissolution processes of d-Fe in aerosol particles (Fig. S1. Sakata et al., 2023). Representative Fe species were determined by using macroscopic X-ray absorption near-edge structure (XANES) spectroscopy to identify d-Fe species in aerosol particles, and the relationship between Fe_{sol}% and Fe species was then investigated. Furthermore, the spot analyses of Fe species in mineral dust and anthropogenic aerosols were performed through microfocused XANES combined with X-ray fluorescence mapping (μ-XRF-XANES) to assess the alteration processes of Fe. Finally, dissolution kinetic models optimized for Fe in mineral dust and anthropogenic aerosols were used to identify the effect of pH on Fe dissolution from these aerosols. The influence of the Fe source (mineral-Fe or anthro-Fe) on Fe_{sol}% in aerosol particles transported to the North Pacific was evaluated independently from the results.

2. Material and Methods

2.1. Aerosol sampling.

NOTOGRO is located in Suzu City in the coastal region of the Sea of Japan, Japan (37.4513°N, 137.3589°E; Fig. 1). The city lacks industrial or other anthropogenic emission sources. Size-fractionated aerosol samples were collected by employing a high-volume air sampler (Model-120, Kimoto, Japan) equipped with a Sierra-type cascade impactor (TE-236, Tisch Environmental Inc., the USA). The air sampler was installed on a rooftop 10 m above ground level. Aerosol particles were collected separately in seven fractions (>10.2, 4.2–10.2, 2.1–4.2, 1.3–2.1, 0.69–1.3, 0.39–0.69, and <0.39 μm) with a flow rate of 0.566 m^3 min^{-1}. Custom-made polytetrafluoroethylene (PTFE) membrane filters (PF050, Advantech, Japan, Sakata et al., 2018, 2021) were used as the sampling filters for all fractions. PTFE filters are not properly wetted by cleaning solutions because they are hydrophobic. This situation has the potential to reduce cleaning efficiency. Therefore, the filters were hydrophilized with ethanol (99.5%, Wako First Class, Wako, Japan). The hydrophilized PTFE filters were soaked in 1 mol L^{-1} hydrochloric acid (EL grade, Kanto Chemical Co. Inc., Japan) and heated at 180 °C for one day. Subsequently, the filters were placed in ultrapure water and heated at 180 °C for one day. The rinsed filters were then air-dried in a clean booth. Air drying

restored the hydrophobicity of the PTFE filters as a result of the complete removal of ethanol from the filters. The rinsed and dried PTFE filters were stored in polyethylene bags. The blank Fe concentration in the PTFE filters was 0.438 ± 0.713 ng cm^{-2} for acid digestion and 0.044 ± 0.040 ng cm^{-2} for ultrapure water extraction. These blank concentrations were at least an order of magnitude lower than the blank Fe concentration in cellulose filters (Morton et al., 2013; Sakata et al., 2018). The filter blanks for Fe at the average sampling flow in this study (approximately 5000 m^3) was less than 0.1 pg m^{-3} and had a negligible effect on the Fe concentration in the aerosol samples.

Aerosol samples were collected monthly from July 2019 to June 2020 (Table S1). On the basis of backward and forward trajectory analyses, this study categorized aerosol samples into two groups (Figs. S2 and S3). The first group included samples collected during the Japanese air mass (JPN) period (July–October 2019 and May–June 2020). Air masses arriving at the sampling site (NOTOGRO) during the JPN period originated from the domestic region of Japan and its marginal sea (Fig. S2a). In addition, forward trajectory analyses indicated that these air masses were not transported to the North Pacific Ocean (Fig. S3a). The second group included the samples collected during the East Asian outflow (EAout) period (November 2019–April 2020; seasons: winter and spring). During the EAout period, air masses arriving at the sampling site originated from East Asia and were subsequently transported to the Pacific Ocean (Figs. S2b and S3b).

The aerosol filters were folded in half immediately after sampling. The folded filters were then placed in polyethylene bags and stored in a desiccator with RH below 20% until analysis. In China, the COVID-19 lockdown was imposed from January 23 to February 19, 2020 (Liu et al., 2021; Li et al., 2021; Zheng et al., 2020; Xu et al., 2022). Therefore, the aerosol samples collected in January and February were considered as having been collected during and after the COVID-19 lockdown period, respectively (Table S1).

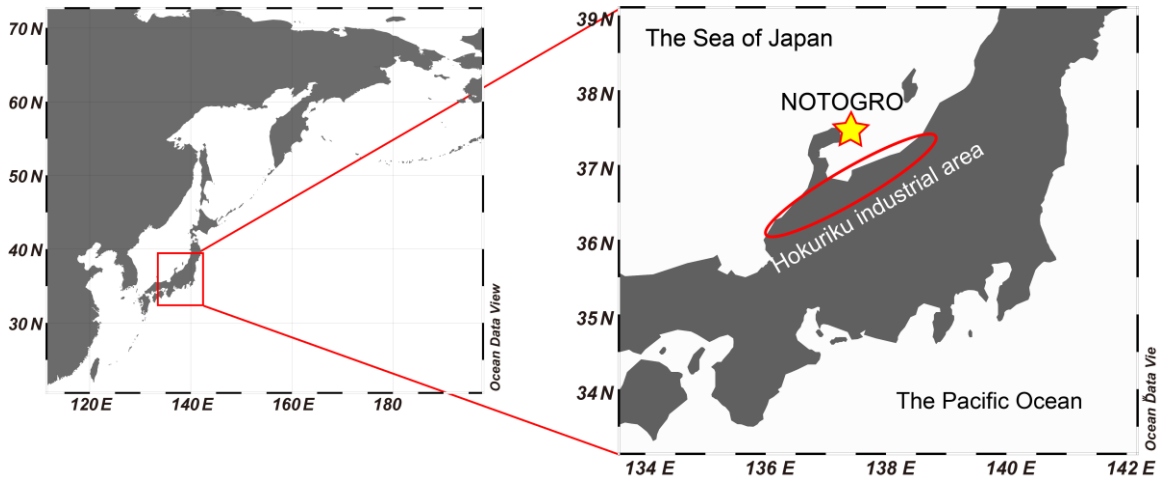

Figure 1. Sampling site (NOTOGRO) for size-fractionated aerosols. The figure was described using Ocean Data View (Schlitzer, 2023).

2.2. Determinations of total and dissolved metal concentrations

The Fe concentration measured after the complete acid digestion of aerosol particles is denoted as T-Fe (= d-Fe + insoluble Fe). Approximately one-fifth of the collected aerosol sample in each size fraction was decomposed by using an acid mixture (2 mL of 15.5 mol L^{-1} HNO_3, 2 mL of 11.3 mol L^{-1} HCl, and 1 mL of 28 mol L^{-1} HF, ultrapure AA 100, Kanto Chemical, Co., Inc., Japan) in perfluoroalkoxy alkane vials by heating at 150 °C for one day. The mixed acid was evaporated to dryness, and the evaporated residue was redissolved in 2% HNO_3. The solutions were filtrated by using a syringe filter made of hydrophilic polyethersulfone (PES, Millex, ϕ: 0.45 μm, Merck, Germany).

Dissolved Fe in aerosol particles was extracted with 2–4 mL of ultrapure water in a polypropylene centrifuge tube and horizontal shaking for one day. After being subjected to water extraction, the PTFE filter was removed from the vial, and the solution was filtered through a PES syringe filter. The filtrated solutions were evaporated to dryness. The evaporated residue was then redissolved in 2% HNO_3. Elemental concentrations were determined by using an HR-ICP-MS (Elemental II, Germany). The precision and accuracy of the quantification of target elements were confirmed through the repetitive analysis of the reference material of urban aerosols (Table S2, NIES CRM 28. Urban aerosol, Mori et al., 2008). All sample treatments described above were performed in a clean room (class 1000).

The enrichment factor of Fe ($EF_{T\text{-}Fe}$) normalized by the mass ratio of Fe relative to that of Al in the upper continental crust (UCC) was calculated to evaluate the emission sources of Fe. The following equation was used for the calculation:

$$EF_{\mathrm{T-Fe}} = \frac{(\mathrm{T-Fe/T-Al})_{aerosol}}{(\mathrm{T-Fe/T-Al})_{UCC}}, \quad \text{(Eq. 1)}$$

where $(T\text{-}Fe/T\text{-}Al)_{aerosol}$ represents the mass concentration of total Fe (= insoluble Fe + d-Fe in aerosol particles relative to the total Al). In this study, in consideration of the variation in the T-Fe/T-Al ratio in the UCC, the average value from five sources in the literature (=0.52 ± 0.12) was used (Turkian and Wedepohl, 1961; Taylor, 1964; Wedepohl, 1995; Taylor and McLennan, 1995; Rudnick and Gao, 2003). The contribution of anthro-Fe has traditionally been considered remarkable when $EF_{T\text{-}Fe}$ exceeds 10. However, recent studies have indicated a narrow range of T-Fe/T-Al ratios for Asian dust (T-Fe/T-Al: 0.56 ± 0.17, X. Liu et al., 2022; Sakata et al., 2023). Consequently, a significant contribution of anthro-F) to T-Fe in aerosol particles was identified when $EF_{T\text{-}Fe}$ exceeds 2.0 (T-Fe/T-Al > 1.04). In addition to $EF_{T\text{-}Fe}$, T-Fe concentrations associated with mineral dust and anthro-Fe were estimated by using the following equations:

$$Mineral\ Fe = Aerosol\ Al \times (T-Fe/T-Al)_{crust}, \quad \text{(Eq. 2)}$$

$$Anthropogenic\ Fe = Aerosol\ Fe - Mineral\ Fe, \quad \text{(Eq. 3)}$$

2.3. Source apportionment of T-Fe and d-Fe

2.3.1. Diagram between $EF_{T\text{-}Fe}$ and [d-Fe]/[d-Al]

A diagram of [d-Fe]/[d-Al] ratios combined with $EF_{T\text{-}Fe}$ are useful tools for evaluating the sources and dissolution processes of d-Fe in aerosol particles because the Fe_{sol}% values of aerosol particles vary depending on the dominant sources of T-Fe and d-Fe (Sakata et al., 2023). T-Fe and d-Fe sources can be categorized into the following five groups (Fig. 2): T-Fe in groups (i)

and (ii) originate from mineral dust with $EF_{T\text{-}Fe}$ < 2.0. The [d-Fe]/[d-Al] ratio varies depending on the different dissolution processes of mineral dust (i.e., proton- and ligand-promoted dissolution processes). The [d-Fe]/[d-Al] ratio for ligand-promoted dissolution ([d-Fe]/[d-Al] > 1.0) is higher than that for proton-promoted dissolution ([d-Fe]/[d-Al]: 0.1–1.0) because Fe is preferentially dissolved by organic ligands over Al. T-Fe in groups (iii) and (iv) is derived from anthro-Fe with $EF_{T\text{-}Fe}$ > 2.0. In group (iii), T-Fe is mainly derived from anthro-Fe, whereas d-Fe is derived from mineral dust because anthro-Fe is present in the form of insoluble Fe, which cannot affect the [d-Fe]/[d-Al] ratio of aerosol particles. By contrast, the anthro-Fe in group (iv) is highly soluble, and its high T-Fe/T-Al ratio (i.e., high $EF_{T\text{-}Fe}$) is retained upon dissolution, as reflected by its [d-Fe]/[d-Al] ratio. Consequently, aerosols in group (iv) exhibit high $EF_{T\text{-}Fe}$ and [d-Fe]/[d-Al]. However, distinguishing between proton- and ligand-promoted dissolutions is difficult because highly soluble anthro-Fe exhibits high [d-Fe]/[d-Al] ratios in both processes. Herein, anthro-Fe refers to anthropogenic Fe-rich particles that can increase the $EF_{T\text{-}Fe}$ emitted from not only high-temperature combustion (e.g., steel industry and coal combustion; Kajino et al., 2020; Ito et al., 2021), but also non-combusted anthro-Fe (e.g., non-exhaust vehicle particles, such as brake ring and tire wear debris; Sanderson et al., 2016; Li et al., 2022; Fu et al., 2023). Finally, group (v) consists of aluminosilicate glasses emitted from high-temperature combustion, including coal combustion and municipal solid waste incineration. These particles are characterized by low $EF_{T\text{-}Fe}$ values (<2.0) and [d-Fe]/[d-Al] ratios (<0.1). A detailed description of these five classifications is presented in S.1.1 in Supplemental Information.

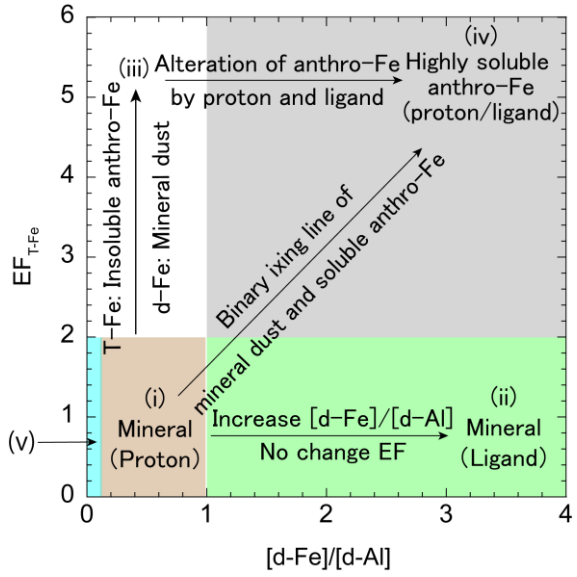

Figure 2. Diagram of $EF_{T\text{-}Fe}$ and the [d-Fe]/[d-Al] ratio for evaluating the T-Fe and d-Fe sources of aerosol particles.

As detailed in Section 3.3.2, the d-Fe in fine aerosol particles was composed of a binary mixture of d-Fe dissolved through the proton-promoted dissolution of mineral dust and highly soluble anthro-Fe. Herein, the contribution of anthro-Fe to d-Fe

(F_{anthro}) in fine aerosol particles was estimated on the basis of a two-component mixing model by using the following equations (Sakata et al., 2023):

$$F_{mineral} + F_{anthro} = 1, \text{(Eq. 4)}$$

$$\left(\frac{[d-Fe]}{[d-Al]}\right)_{aerosol} = \left(\frac{[d-Fe]}{[d-Al]}\right)_{mineral} \times F_{mineral} + \left(\frac{[d-Fe]}{[d-Al]}\right)_{anthro} \times F_{anthro}, \text{(Eq. 5)}$$

The average [d-Fe]/[d-Al] ratio of coarse aerosol particles (=0.28) was the representative value of ([d-Fe]/[d-Al])$_{mineral}$. The representative [d-Fe]/[d-Al] ratio of anthro-Fe was 2.18, which was the average [d-Fe]/[d-Al] ratio of fine aerosol particles with a value higher than 1.50 (Sakata et al., 2023). Concentrations of d-Fe associated with mineral dust and anthro-Fe were calculated by employing the following equations:

$$\text{Mineral d} - \text{Fe} = \text{d} - \text{Fe} \times F_{mineral}, \quad \text{(Eq. 6)}$$

$$\text{Anthropogenic d} - \text{Fe} = \text{d} - \text{Fe} \times F_{anthro}, \quad \text{(Eq. 7)}$$

Subsequently, the Fe_{sol}% of mineral dust (mineral-Fe_{sol}%) was calculated by dividing mineral d-Fe by mineral Fe through the same approach as that employed for the calculation of anthro-Fe (anthro-Fe_{sol}%).

2.3.2. PMF

T-Fe and d-Fe sources in fine aerosol particles were also evaluated through PMF (EPA PMF version 5.0, Norris et al., 2014). PMF analyses were performed separately for the entire sampling period (JPN+EAout) and the JPN and EAout periods. The PMF analysis for the JPN+EAout period was conducted to evaluate the monthly trend of the normalized contribution of each factor, with the average of all contributions for each factor normalized to 1. By contrast, PMF analyses were performed separately for the JPN and EAout periods to evaluate the average $EF_{T\text{-}Fe}$, Fe_{sol}%, and [d-Fe]/[d-Al] ratios of each factor. These analyses used fine aerosol particles collected during the respective periods. The concentrations of Na, Mg, Al, d-Al, K, Ca, Ti, V, Cr, Mn, Fe, anthro-Fe, d-Fe, Co, Ni, Cu, Zn, Sr, Cd, Ba, Pb, and SO_4^{2-} in the <0.39, 0.39–0.69, and 0.69–1.3 μm fractions were used as the input data for PMF analysis. A detailed descriptions of PMF method are described in S.1.2 in Supplemental Information.

2.4. Macroscopic and micro-focused XANES.

As the macroscopic and microscopic XANES techniques applied herein are consistent with those reported by Sakata et al. (2022) and Sakata et al. (2021), their description will be kept brief. The experiments for macroscopic (beamline: BL-9A and BL-12C) and semi-microscopic XANES (beamline: BL-15A) were performed at Photon Factory, High Energy Acceleration Research Organization, Ibaraki, Japan. The details of the optics and experimental set-up for the macroscopic and semi-microscopic experiments are described in the Supplemental Information. The aerosol samples, initially collected on PTFE filters, were transferred onto carbon tape, then mounted at a 45° angle relative to the incoming X-ray beam. In microscopic and semi-microscopic analyses, XANES spectra were acquired via the fluorescence yield technique, with a silicon drift detector used to detect fluorescence X-rays from samples. Specifically for semi-microscopic experiments, XRF mapping was

performed first, and then Fe K-edge XANES spectra at the regions of interest were obtained. The linear combination fitting of the samples was conducted against the same standards reported by Sakata et al. (2022). A detailed descriptions of PMF method are described in S.1.3 in Supplemental Information.

2.5. Estimation of dissolution pH of mineral dust and anthro-Fe

2.5.1. Dissolution pH of mineral dust

Aerosol particles are repeatedly incorporated into and re-emitted from cloud water in the atmosphere (aerosol–cloud cycles), with Fe dissolution primarily occurring in highly acidic aerosol phases (Spokes et al., 1994; Shi et al., 2015; Maters et al., 2016). Given that the dissolution of Fe in mineral dust occurs in the aerosol phase (pH < 3.0), Fe dissolution from mineral dust was simulated by using the three-Fe pool model (Shi et al., 2011a; Sakata et al., 2022). The fast Fe (ferrihydrite and poorly crystalline Fe oxides), intermediate Fe (Fe oxide nanoparticles), and slow Fe (crystalline Fe oxides and aluminosilicates) pools represent three Fe pools with different dissolution rates (k, Table 1). Shi et al. (2011a) reported that the dissolution rate of the slow Fe pool is similar to that of illite. However, biotite is more abundant than illite in the aerosol samples collected in our present and previous works (Sakata et al., 2022). Given that the dissolution rate of biotite is approximately one order of magnitude higher than that of illite (Bibi et al., 2011; Bray et al., 2015), the dissolution rate of the slow Fe pool was set to be one order of magnitude higher than that in the original model. Under the assumption of a first-order reaction, the molar concentration at a certain time (t) ([d-Fe(t)]) is described in the following equation:

$$[\mathrm{d-Fe}]_{mineral}\ (\mu mol\ g^{-1}) = [\mathrm{d-Fe}]_{\mathrm{fast}} + [\mathrm{d-Fe}]_{\mathrm{intermediate}} + [\mathrm{d-Fe}]_{\mathrm{slow}}, \quad \text{(Eq. 8)}$$

$$[\mathrm{d-Fe}(t)]_{\mathrm{fast}}\ (\mu mol\ g^{-1}) = [\mathrm{d-Fe}]_{mineral} \times [\%\mathrm{FeT}]_{\mathrm{fast}} \times (1 - e^{-kt}), \text{ (Eq. 9)}$$

where $[\mathrm{d\text{-}Fe}]_{\mathrm{mineral}}$ refers to the d-Fe concentration in mineral dust calculated by using Eq. 6. [%FeT] denotes the maximum percentage of Fe that can be solubilized, and k represents the rate constant (h^{-1}). The pH dependence of these parameters is presented in Table 1. The reaction time t was set to 54 h, taking into account atmospheric transport and aerosol–cloud cycles (Sakata et al., 2023). Finally, the pH value for which the sum of d-Fe concentrations across all pools equaled $[\mathrm{d\text{-}Fe}]_{\mathrm{aerosol}}$ was determined.

Table 1 pH dependence of parameters for the three-Fe pool model

Fe pool	[%FeT] (%)	Dissolution rate (h^{-1})
Fast	pH 1.0–2.0: Fixed at 0.9% pH 2.0–3.0: [%FeT] = −0.4 × pH +1.7	$\log k_{\mathrm{fast}} = -0.50 \times \mathrm{pH} + 1.87$
Intermediate	pH 1.0–2.0: Fixed at 3.0% pH 2.0–3.0: [%FeT] = −2.0 × pH + 7.0	$\log k_{\mathrm{intermediate}} = -0.66 \times \mathrm{pH} + 0.36$
Slow	pH 1.0–3.0: [%FeT] = −15.2 × pH + 58.4	$\log k_{\mathrm{slow}} = -0.44 \times \mathrm{pH} - 0.76$

2.5.2. Dissolution pH for anthro-Fe

By using hematite nanoparticles as a proxy for anthro-Fe, the dissolution pH of anthro-Fe was estimated under the assumption that anthro-Fe dissolution is solely driven by proton-promoted dissolutions. Under the assumption that the solid-to-liquid ratio of anthro-Fe is 0.06 g L^{-1}, which is comparable to that of mineral dust, the aerosol liquid water (ALW) content associated with hematite nanoparticles was quantified by using the following equation:

$$ALW\ (L\ m^{-3}) = \frac{Anthro{-}Fe\ concentration/0.699}{0.06\ (=\frac{S}{L}ratio)}, \text{(Eq. 10)}$$

where 0.699 is the mass fraction of Fe in hematite nanoparticles, and anthro-Fe concentrations were estimated by using Eq. 3. The pH dependence of anthro-Fe_{sol}% in ALW under the equilibrium state was estimated on the basis of the solubility product of hematite nanoparticles (Bonneville et al., 2004). The proton-promoted dissolution of hematite nanoparticles and the solubility product ($^{*}K_{so}$ = 0.52) of this reaction are described as:

$$\frac{1}{2}Fe_2O_3 + 3H^{+}_{(aq)} \leftrightarrow Fe^{3+}_{(aq)} + \frac{3}{2}H_2O, \text{(Eq. 11)}$$

$$log\ {}^{*}K_{SO} = log[a_{Fe^{3+}}] + npH, \text{(Eq. 12)}$$

where n is the reaction order determined in a previous study (n: 2.85, Bonneville et al., 2004). The $[a_{Fe^{3+}}]$ represents the activity of Fe^{3+} in the ALW. To simplify the calculations, the activity coefficient is 1, which means that the $[a_{Fe^{3+}}]$ is considered to be equal to the Fe concentration in the solution (nmol L^{-1}). The $[a_{Fe^{3+}}]$ in ALW at each pH was calculated by substituting pH values into Equation 12. Subsequently, the anthro-Fe_{sol}% at equilibrium was calculated for various pH values using the following equation.

$$Equilibrium\ anthro - Fe_{sol}\% = \frac{ALW\ (L\ m^{-3}) \times [a_{Fe^{3+}}]\ (nmol\ L^{-1})}{anthropogenic\ Fe\ (ng\ m^{-3})} \times 100, \text{(Eq. 13)}$$

The pH at which the equilibrium anthro-Fe_{sol}% matched the actual anthro-Fe_{sol}% was determined and defined as the dissolution pH of anthro-Fe.

3. Results and Discussion

3.1. Monthly variation and size distributions of T-Fe and $EF_{T\text{-}Fe}$

The atmospheric T-Fe concentration of total suspended particulates (TSPs: sum of the all size fractions) ranged from 15.6 ng m^{-3} to 312 ng m^{-3} (Fig. 3a, average ± standard deviation [avg ± 1σ: 113 ± 108 ng m^{-3}]). Coarse aerosol particles (>1.3 μm) accounted for 84.8% ± 5.6% of the T-Fe concentration of TSPs (Fig. 3a). The concentrations of T-Fe and typical mineral elements (i.e., Al, Ti, and non-sea-salt Ca^{2+}) were higher in February–April than in other seasons due to the long-range transportation of Asian dust (Figs. 3a and S4, Uematsu et al., 1983; Zhu et al., 2020; Kawai et al., 2021). The annual average of $EF_{T\text{-}Fe}$ of TSP samples was 1.3 ± 0.3 (Fig. 3a), which was identical to that of coarse aerosol particles ($EF_{T\text{-}Fe}$: 1.3 ± 0.4, Fig. 3b). This result indicated that T-Fe in TSPs and coarse aerosol particles was mainly derived from mineral dust.

The T-Fe concentrations of fine aerosol particles (sum of the <0.39, 0.39–0.69, and 0.69–1.3 μm fractions) varied from 4.1 ng m^{-3} to 31.7 ng m^{-3} (avg ± 1σ: 14.0 ± 10.2 ng m^{-3}, Fig. 3a). The annual average of $EF_{T\text{-}Fe}$ was 2.2 ± 1.0, indicating that anthro-Fe was a source of T-Fe in fine aerosol particles (Fig. 3b). The highest $EF_{T\text{-}Fe}$ was usually found in the 0.39–0.69 μm size fraction, indicating that the relative contribution of anthro-Fe to T-Fe in fine aerosol particles was the largest (Fig. 3b). This result agreed with the findings of previous studies that used the Fe isotope ratio (Kurisu et al., 2016). The $EF_{T\text{-}Fe}$ of the fine aerosol particles showed distinct seasonal variations, with higher values during the JPN period (2.9 ± 0.8) than during the EAout period (1.5 ± 0.5; Fig. 3b). This result indicated that the relative abundance of anthro-Fe to that of T-Fe in fine aerosol particles was higher during the JPN period than during the EAout period likely due to the greater contribution of Asian dust in spring than that in other seasons (Fig. 3a). However, the lower relative abundance of anthro-Fe to that of T-Fe did not necessarily indicate a low absolute concentration of anthro-Fe. Indeed, the absolute anthro-Fe concentration of fine aerosol particles during the JPN period (avg ± 1σ: 6.6 ± 5.6 ng m^{-3}, range: 2.8–16.4 ng m^{-3}) was slightly lower than the anthro-Fe concentration during the EAout period, excluding the lockdown period (avg ± 1 σ: 8.2 ± 4.1 ng m^{-3}, range: 0–14.0 ng m^{-3}). The reduction in anthro-Fe concentration by the limitation of human activities during the COVID-19 lockdown period highlighted the importance of anthro-Fe as a source of Fe in fine aerosol particles. The $EF_{T\text{-}Fe}$ of the fine aerosol particles during the COVID-19lockdown period (January 2019, $EF_{T\text{-}Fe}$: 0.5) was lower than those during the periods of pre-lockdown (December 2019, $EF_{T\text{-}Fe}$: 1.9) and post-lockdown (February 2020, $EF_{T\text{-}Fe}$: 1.4, Fig. 3b). Similarly, in Hangzhou, China, the $EF_{T\text{-}Fe}$ of $PM_{2.5}$ during the COVID-19 lockdown period ($EF_{T\text{-}Fe}$: 1.6) was considerably lower than those during the periods of pre-lockdown ($EF_{T\text{-}Fe}$: 13.3) and post-lockdown ($EF_{T\text{-}Fe}$: 6.6, Liu et al., 2021). The decrease in $EF_{T\text{-}Fe}$ was attributed to the decrease in the emission of Fe-rich particles from non-exhaust vehicle sources (Li et al., 2022), which, in turn, were emitted from the abrasion processes of brake rings and tire wear. Furthermore, the Fe concentrations in $PM_{2.5}$ collected in Tangshan and Wuhan decreased because of the reduction in anthropogenic emissions, including those from the steel industry (Zheng et al., 2020; Xu et al., 2022). Therefore, anthro-Fe was a dominant source of Fe in fine aerosol particles in East Asia under normal conditions.

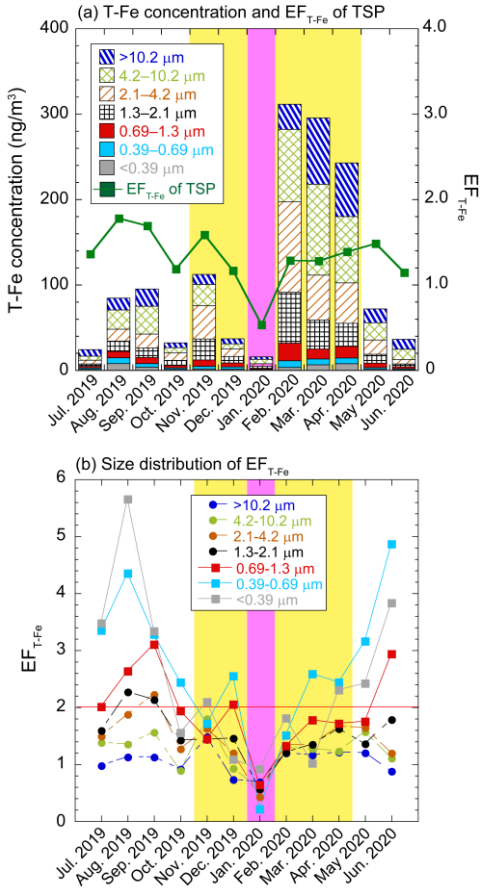

Figure 3. (a) Monthly variations in T-Fe concentration and EF_{T-Fe} in TSPs and (b) size distributions of EF_{T-Fe} (red line: EF_{T-Fe} = 2.0). The data of coarse aerosol particles are shown in dashed boxes or lines, whereas those of fine aerosol particles are described in solid boxes or lines. Yellow and pink shaded regions show the EAout and COVID-19 lockdown periods, respectively.

3.2. Monthly variations and size distributions of d-Fe, Fe_{sol}%, and [d-Fe]/[d-Al] ratio

3.2.1. Coarse aerosol particles

The d-Fe concentrations and Fe_{sol}% of TSPs varied from 0.6 ng m^{-3} to 14.7 ng m^{-3} (avg ± 1σ: 6.3 ± 4.0 ng m^{-3}) and 2.8% to 17.4% (avg ± 1σ: 8.3% ± 5.3%), respectively (Fig. 4a). The seasonal average Fe_{sol}% of TSPs for the EAout period (avg ± 1σ: 4.9% ± 4.3%) were lower than those for the JPN period (avg ± 1σ: 11.6% ± 4.2%). Consistent with those of the TSP samples collected during the EAout period, the Fe_{sol}% of TSPs collected over the Pacific Ocean were typically 1.0%–10% (Table S3). In line with previous observations in Japan (Sakata et al., 2023, Takahashi et al., 2013), the d-Fe concentration of the TSPs decreased from August to January, then increased from January to June (Fig. 4a). The d-Fe concentration of TSPs

from July 2019 to January 2020 was controlled by factors that affected Fe_{sol}% (e.g., emission sources and chemical alterations of Fe-bearing particles) considering that d-Fe concentration and $Fe_{sol\%}$ showed monthly variations during this period (Fig. 4a). By contrast, the d-Fe concentrations of TSPs collected from February to April were considerably higher than those of the samples collected in January, whereas the Fe_{sol}% of TSPs collected from February to April were almost the same as that of the samples collected in January (Fig. 4a). In this case, the atmospheric concentration of d-Fe increased because of the large mineral dust load in the atmosphere.

The Fe_{sol}% of coarse aerosol particles (avg ± 1σ: 2.2% ± 3.0%, range: 0.1%–13.6%) was slightly higher than that of typical mineral dust (<1%, Fig. 4b). The [d-Fe]/[d-Al] ratio of coarse aerosol particles (avg ± 1σ: 0.28 ± 0.12, range: 0.13–0.82) was in line with that of d-Fe dissolved from Asian dust through proton-promoted dissolution (0.24 ± 0.20, Figs. 5a and 5b), indicating that d-Fe in coarse aerosol particles mainly originated from the proton-promoted dissolution of mineral dust. Indeed, the Fe_{sol}% of coarse aerosol particles was correlated with the [nss-SO_4^{2-}]/[T-Fe] ratio as an indicator of the acidity of Fe-bearing particles (Fig. S5a; Zhu et al., 2020, 2022; Liu et al., 2022). Furthermore, the Fe_{sol}% of coarse aerosol particles increased with decreasing aerosol diameter because of the increase in specific surface area, which is a factor controlling aerosol reactivity (Fig. 4b). A similar result was obtained by an observational study at Higashi-Hiroshima, Japan (Sakata et al., 2023). Therefore, Fe % in coarse aerosol particles collected at NOTOGRO is mainly governed by proton-promoted dissolutions.

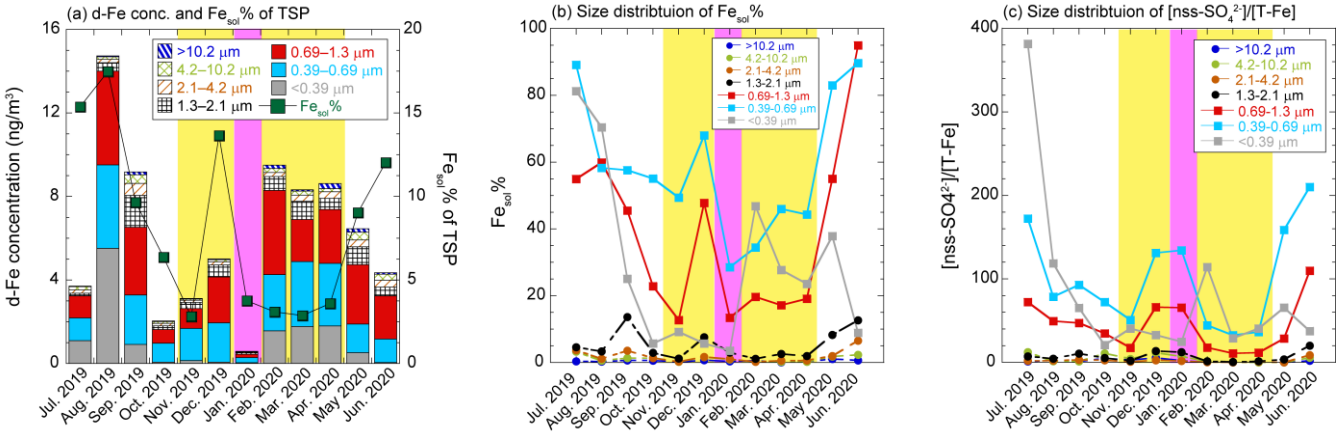

Figure 4. (a) d-Fe concentration and Fe_{sol}% of TSPs; (b) Fe_{sol}%; and (c) the [nss-SO^4_{2-}]/[T-Fe] ratio. The data of coarse aerosol particles are shown in dashed boxes or lines, whereas those of fine aerosol particles are presented in solid boxes or lines. Yellow and pink areas indicate the EAout and COVID-19 lockdown periods, respectively.

3.2.2. Fine aerosol particles

The summation of d-Fe in fine aerosol particles varied from 0.5 ng m^{-3} to 14.0 ng m^{-3} (avg ± 1σ: 5.3 ± 3.7 ng m^{-3}), accounting for 71.1%–94.8% (avg ± 1σ: 81.7% ± 7.0%) of d-Fe in TSPs (Fig. 4a). The Fe_{sol}% of each size fraction of fine aerosol particles (avg ± 1σ: 42.1% ± 25.6%, range: 4.1%–94.9%) was an order of magnitude higher than that of coarse aerosol particles (Fig. 4b). As mentioned above, the Fe_{sol}% of our TSP samples was identical to that of Pacific aerosol (Table S3), and

the size distribution of the Fe_{sol}% of our samples agreed with that reported by previous observational studies conducted in East Asia and the Pacific Ocean (Sakata et al., 2022, 2023; Kurisu et al., 2024). Therefore, fine aerosol particles transported from East Asia play an essential role in the supply of d-Fe to the North Pacific Ocean. Chemical alterations, including aerosol acidification, was a factor increasing the Fe_{sol}% of fine aerosol particles because the Fe_{sol}% of fine aerosol was correlated with the molar ratio of non-sea-salt sulfate to that of T-Fe ([nss-SO_4^{2-}]/[T-Fe]; Fig. S5b). Fe-bearing particles in fine aerosol particles were more acidified than those in coarse aerosol particles considering that the annual average of the [nss-SO_4^{2-}]/[T-Fe] ratio of fine aerosol particles (avg ± 1σ: 75 ± 71, range: 11–381) was higher than that of coarse aerosol particles (avg ± 1σ: 4 ± 5, Fig. 4c). The average [nss-SO_4^{2-}]/[T-Fe] ratio for the JPN period (avg ± 1σ: 101 ± 87) was higher than that for the EAout period (avg ± 1σ: 50 ± 39; Fig. 4c). This result indicated that consistent with the higher Fe_{sol}% in the JPN period than that in the EAout period, the fine aerosol particles collected during the JPN period were more acidified than those collected during the EAout period.

The [d-Fe]/[d-Al] ratio in fine aerosol particles ranged from 0.14 to 3.78 (avg ± 1σ: 1.18 ± 0.77, Fig. 5a), with these values being higher than those in coarse aerosol particles (Fig. 5b). Factors potentially contributing to an increased [d-Fe]/[d-Al] ratio in aerosols include ligand-promoted Fe dissolution from mineral dust and the contribution of anthro-Fe to d-Fe. However, considering the absence of aerosol samples in area (iv) as illustrated in Fig. 5b, ligand-promoted dissolution was not the primary cause of the high [d-Fe]/[d-Al] ratio in fine aerosol particles. Therefore, the elevated [d-Fe]/[d-Al] ratio in fine aerosol particles is primarily attributed to the influence of anthro-Fe. Indeed, the data for fine aerosol particles plotted along the mixing line between proton-promoted dissolution of mineral dust and highly soluble anthro-Fe (Fig. 5b) indicate that these two processes are dominant sources of d-Fe. The significant contribution of d-Fe from highly soluble anthro-Fe was further supported by the correlation between $EF_{T\text{-}Fe}$ and Fe_{sol}% of fine aerosol particles (Fig. 5c). Furthermore, observations during the COVID-19 lockdown period provide crucial insights into the importance of anthro-Fe as a source of d-Fe under normal conditions. This is because the [d-Fe]/[d-Al] ratio in fine aerosol particles collected during the lockdown period was similar to that of mineral dust (pink diamonds in Fig. 5b), suggesting a reduced influence of anthropogenic sources on d-Fe during the lockdown.

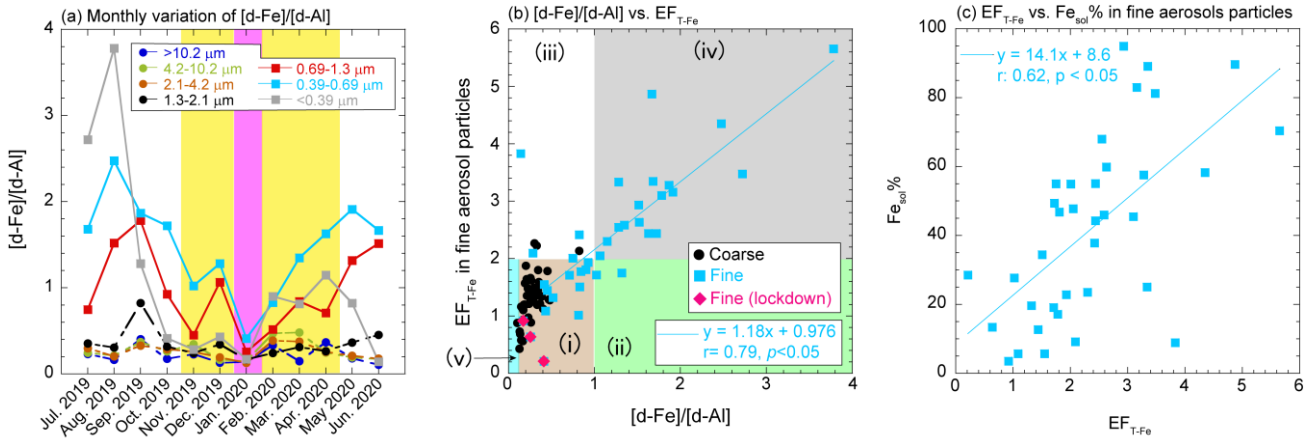

Figure 5. (a) Size distribution of the [d-Fe]/[d-Al] ratio. Yellow and pink areas indicate the EAout and COVID-19 lockdown periods, respectively. (b) relationships of $EF_{T\text{-}Fe}$ and the [d-Fe]/[d-Al] ratio. The background color indicates the emission sources of T-Fe and d-Fe, which are detailed in Fig. 2. (c) Correlation between $EF_{T\text{-}Fe}$ and Fe_{sol}%.

The annual average F_{anthro} of fine aerosol particles was 46.2% ± 26.3% (range: 1.4%–100%) and was higher during the JPN period than during the EAout period (Fig. 6a). Consistent with the results from previous studies using [d-Fe]/[d-Al] and Fe isotope ratios (Kurisu et al., 2016; Sakata et al., 2023), T-Fe in the 0.39–0.69 μm fraction was most influenced by anthro-Fe due to the highest F_{anthro} (Fig. 6a). The seasonal average F_{anthro} values of TSPs collected during the JPN and EAout periods were 33.7% ± 20.9% and 16.6% ± 9.6%, respectively. The lower F_{anthro} of TSPs than of fine aerosol particles was attributed to the large contribution of mineral dust in coarse aerosol particles, especially during the EAout period. A similar result has been reported by a previous study performed in Higashi-Hiroshima, Japan, in 2013 (range: 1.5%–80.7%, JPN: 29.4% ± 25.8%, EAout: 13.5% ± 10.6%, Sakata et al., 2023). Although annual anthro-Fe emissions in China are an order of magnitude higher than those in Japan (Kajino et al., 2020), the lower F_{anthro} in the EAout period compared with that in the JPN period can be ascribed to the extensive emission of mineral-Fe, especially in spring. Therefore, although mineral dust was the most dominant source of d-Fe in TSPs collected at the eastern end of East Asia, the contribution of anthro-Fe to d-Fe was not negligible.

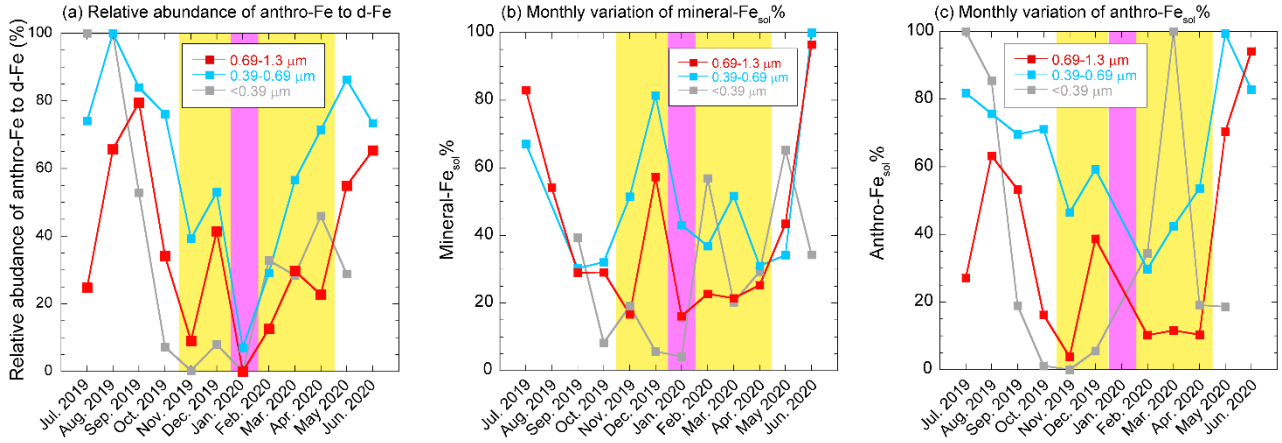

Figure 6. Monthly trends of the relative abundances of anthro-Fe to those of (a) d-Fe, (b) mineral-Fe_{sol}%, and (c) anthro-Fe_{sol}% in fine aerosol particles. Yellow and pink shaded regions show the EAout and COVID-19 lockdown periods, respectively. The plots of anthro-Fe_{sol}% in panel (c) are missing because either or both anthro-Fe or anthro-dFe concentrations were 0 due to the remarkable but small contributions of anthro-Fe during the COVID-19 lockdown period.

3.3. Fe_{sol}% of mineral dust and anthropogenic aerosols

The annual average of mineral-Fe_{sol}% (40.5% ± 24.8%) was considerably higher than the Fe_{sol}% of coarse aerosol particles (Fig. 6b). Given that the Fe_{sol}% of mineral dust at emission is typically less than 1% regardless of aerosol diameter (Shi et al., 2011b), the high mineral-Fe_{sol}% values of fine aerosol particles were caused by the severe chemical alteration, including proton-promoted dissolution, of mineral dust. Indeed, mineral-Fe_{sol}% was correlated with [nss-SO_4^{2-}]/[T-Fe] ratios, which were plotted on an extension of the approximate line for coarse aerosol particles (Fig. S6a). This result indicated that similar to that in coarse aerosol particles, mineral dust in fine aerosol particles underwent alteration processes. However, the extent of aerosol acidification differed between coarse and fine aerosol particles. Although mineral dust in fine aerosol particles exhibited high Fe_{sol}%, the annual average mineral-Fe_{sol}% of TSPs was only 4.4% ± 2.3% (range: 1.9%–9.5%) owing to the low Fe_{sol}% of mineral dust in coarse aerosol particles. This finding emphasized the importance of the proton-promoted dissolution of mineral dust in fine aerosol particles for the d-Fe supply via mineral dust deposition. Notably, ligand-promoted dissolution is considered a process that increases the Fe_{sol}% of mineral dust. However, the contribution of ligand-promoted Fe dissolution was likely small because there were almost no plots of aerosol particles in region (ii) of Fig. 5b, a region where this process is a major contributor to mineral dust.

The annual average of anthro-Fe_{sol}% was 46.7% ± 32.9% and was higher in the JPN period than in the EAout period (Fig. 6c). Anthro-Fe_{sol}% can be enhanced not only by the chemical alteration of anthropogenic aerosols but also by the direct emission of highly soluble anthro-Fe emitted from liquid fuel combustion, including fuel oil and gasoline (Fe_{sol}%: up to 80%, Sedwick et al., 2007; Sholkovitz et al., 2009; Schroth et al., 2009; Oakes et al., 2012). However, the contribution of anthro-Fe from liquid fuel combustion to T-Fe and d-Fe in our samples was not remarkable, as described in the following section (Fig. 7). Therefore, the seasonal variation in anthro-Fe_{sol}% is primarily controlled by the extent of the chemical alterations of anthro-Fe, including aerosol acidification. This finding is supported by the strong correlation between anthro-Fe_{sol}% and the [nss-$SO4^{2-}$]/[T-Fe] ratio (Fig. S6b). Notably, anthro-Fe_{sol}% tended to be higher than mineral-Fe_{sol}% during the JPN period (summer), whereas the opposite was true during the EAout period (winter), with mineral-Fe_{sol}% exceeding anthro-Fe_{sol}% (Figs. S6c–S6e). This shift is likely attributable to the differing sensitivities of mineral-Fe_{sol}% and anthro-Fe_{sol}% to changes in aerosol acidity (further details are discussed in Section 3.7).

3.4. Source apportionment of Fe in fine aerosol particles by PMF

3.4.1. Sources of T-Fe and anthro-Fe

Six factors were identified as sources of fine aerosol particles during the JPN+EAout period: (i) sea spray aerosol and fresh mineral dust (hereafter referred to as fresh dust; Fig. S7a), (ii) aged mineral and road dust (hereafter referred to as aged dust; Fig. S7b), (iii) the steel industry (Fig. S7c), (iv) heavy oil combustion (Fig. S7d), (v) the non-steel industry (Fig. S7e), and (vi) secondary sulfate aerosol and dissolved metals formed through aerosol acidification (hereafter referred to as secondary aerosol; Fig. S7f). Fresh and aged dust factors (factors i and ii) included mineral-Fe and anthro-Fe, such as non-exhaust vehicle particles in road dust. The primary sources of the precursors of secondary sulfate aerosols (factor iv) and metal elements were mainly derived from coal combustion, as indicated by the large contributions of K, Zn, Cd, and Pb as the tracer elements of its

emission. Detailed classification methods, including the tracer elements used for each factor, are described in the Supplemental Information. Several factors grouped into multiple emission sources because of their similar emission processes and/or physicochemical properties. For instance, sea spray aerosols and fresh dust grouped into factor (i). Both are blown by the wind from their sources and are likely to exhibit covarying atmospheric concentrations. Consequently, the PMF model may have limitations in resolving covariant sources (Pindado and Perez, 2011).

Next, PMF analyses were performed individually by using fine aerosol particles collected during the JPN and EAout periods to evaluate the seasonal average contribution of each factor to T-Fe, anthro-Fe, and d-Fe (Figs. 7 and S7). Moreover, the $EF_{T\text{-}Fe}$, Fe_{sol}%, and [d-Fe]/[d-Al] ratio of each factor were estimated by PMF for each period (Tables S4 and S5). The same factors were identified as the dominant sources of fine aerosol particles during the JPN period (Fig. S8). While heavy oil combustion was not identified as a major source of fine aerosol particles during the EAout period, the other five emission sources remained important contributors to the source of fine aerosol particles in this period (Fig. S9). These results are reasonable because the PMF analysis of the JPN+EAout period revealed a small contribution to heavy oil combustion during the EAout period (Fig. S7d). T-Fe in fine aerosol particles during the JPN and EAout periods were mainly derived from the steel industry, then from aged dust, fresh dust, and secondary aerosol (Figs. 7a and 7d). Anthro-Fe in fine aerosol particles collected during the JPN period originated from the steel industry (36.8%) and secondary aerosols associated with high-temperature combustion (27.1%, Fig. 7b). Given that SO_2, a precursor of sulfate aerosols in East Asia, was mainly emitted from coal combustion (Wang et al., 2014; Kurokawa and Ohara, 2020), anthro-Fe in the secondary aerosol factor was also emitted from coal combustion. Non-exhaust vehicle particles in aged and fresh dust contributed to anthro-Fe sources (28.5%, Fig. 7b). Therefore, anthro-Fe in fine aerosol particles originated from high-temperature combustion and non-combusted anthro-Fe. This result is consistent with the anthro-Fe sources in Japanese $PM_{2.5}$ estimated by a semibottom-up model (Kajino et al., 2020): the steel industry (20%–50%), brake pad debris (20%–40%, main components of non-exhaust vehicle particles), and coal-fired power plants (10%–20%). During the EAout period, approximately 80% and 20% of anthro-Fe originated from the steel industry and non-exhaust vehicle particles in aged dust + fresh dust factors, respectively (Fig. 7e). This result was in line with previously reported findings because approximately 90% and 60% of anthropogenic nanoparticles (mainly composed of magnetite) and anthro-Fe were emitted from the steel industry in China, respectively (Li et al., 2021; Chen et al., 2021).

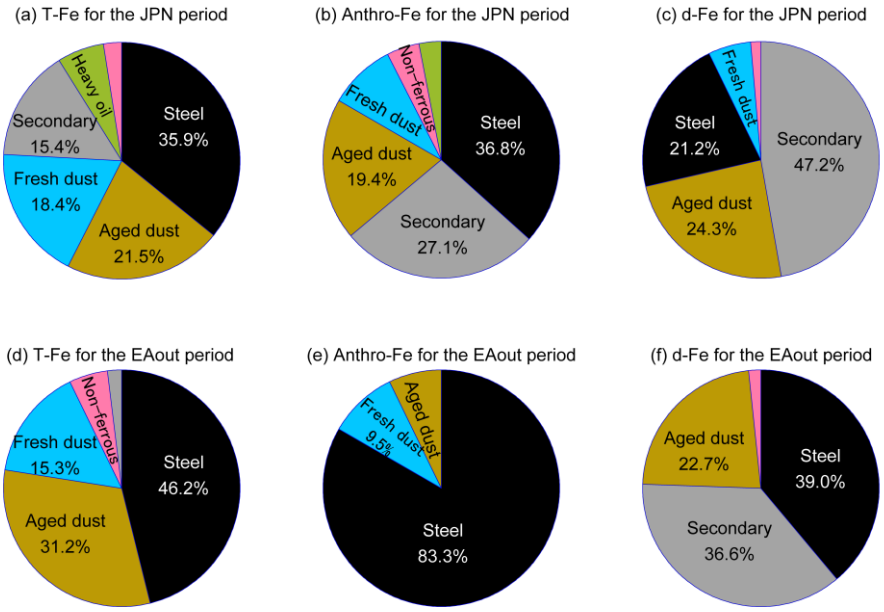

Figure 7. Panels (a-c) show average contributions to T-Fe, anthro-Fe, and d-Fe, respectively, for the JPN period. Panels (d-f) show contributions to T-Fe, anthro-Fe, and d-Fe, respectively, for the EAout period.

As mentioned previously, the contribution of anthro-Fe to T-Fe in fine aerosol particles collected during the COVID-19 lockdown was almost 0 because $EF_{T\text{-}Fe}$ in these samples was less than 1.0 (Fig. 3b). The normalized factor contribution of the steel industry during the COVID-19 lockdown period was significantly lower than those during the pre-lockdown and post-lockdown periods (Fig. S7c). This result indicated that the steel industry was the dominant source of anthro-Fe. The importance of the steel industry as the source of anthro-Fe was emphasized by the reduction in human activities caused by the COVID-19 lockdown considering that the normalized contribution of the steel industry during the lockdown period was considerably lower than that during the pre- and post-lockdown periods.

3.4.2. Sources of d-Fe

PMF analysis indicated that d-Fe in the fine aerosol particles collected during the JPN and EAout periods originated from three primary sources: the steel industry, aged dust, and secondary aerosol formation (Figs. 7c and 7f). The steel industry factor can be characterized by the highest $EF_{T\text{-}Fe}$ (JPN: 3.9, EAout: 4.9). Given that non-atmospherically aged Fe-rich particles collected from the steel plants are likely insoluble (Li et al., 2017), the Fe-rich particle unlikely contributed to increasing the [d-Fe]/[d-Al] ratio without chemical alteration in the atmosphere (Fig. 2). However, the [d-Fe]/[d-Al] ratio in the steel industry factor (JPN: 5.67, EAout: 1.20) is higher than 1.0 and their Fe_{sol}% showed high water solubility (JPN: 31.8%, EAout: 22.4%). Therefore, insoluble Fe-rich particles released from steel plants are thought to transform into d-Fe in the atmosphere. This is supported by the high [nss-SO_4^{2-}]/[T-Fe] ratio of the steel industry factor, despite Fe-rich particles collected at the plants

lacking sulfur (Li et al., 2017; Zhu et al., 2020, 2022). This indicates atmospheric reactions with H_2SO_4, leading to an increased Fe_{sol}% for the steel industry factor.

Moreover, the Fe_{sol}% exhibited by aged dust (JPN: 60.6%, EAout: 19.3%) was considerably higher than that shown by fresh mineral dust (typically less than 1.0%; Shi et al., 2011b), indicating that Fe in the aged dust factor also dissolved through chemical alterations in the atmosphere. The fresh dust factor had a [nss-SO_4^{2-}]/[T-Fe] ratio of 0, whereas the aged dust factor had a high [nss-SO_4^{2-}]/[T-Fe] ratio, indicating that aged dust was subjected to the effects of aerosol acidification by H_2SO_4 (Tables S4 and S5). The [d-Fe]/[d-Al] ratio of the aged dust factor (JPN: 0.92, EAout: 0.69) was within that of mineral dust originating from proton-promoted dissolution but was higher than the average ratio of coarse aerosol particles minimally influenced by aerosol acidification (0.28 ± 0.12). As mentioned above, the aged dust fraction contained non-exhaust vehicle emissions (e.g., brake rings and tire wear debris), which were mainly present in the form of Fe-rich particles, such as Fe oxides (Sanderson et al., 2016; Li et al., 2022; Fu et al., 2023). Given that the Fe_{sol}% values of brake ring and tire wear debris were less than 0.01% in the absence of chemical alterations, including proton- and ligand-promoted dissolutions (Shupert et al., 2013; Halle et al., 2021), the increase in the [d-Fe]/[d-Al] ratio of the aged dust factor may have been caused by the dissolution of Fe from these materials during chemical alterations in the atmosphere. Previous research suggests that tire wear acts as an emission source of d-Fe in $PM_{2.5}$ (Fang et al., 2015), which can be dissolved by SO_2 emitted from coal combustion (Wong et al., 2020). Although further research is needed, our findings indicate that NEV particles, such as brake ring particles, can also be a source of d-Fe via aerosol acidification in the atmosphere.

The considerable contribution of the secondary aerosol factor to d-Fe highlights the importance of aerosol acidification in the dissolution of Fe from fine aerosol particles. As mentioned previously, the secondary aerosol factor is markedly influenced by coal combustion, a primary source of SO_2, and can be a source of d-Fe in aerosol particles. However, d-Fe in the above factor likely originated from not only coal combustion but also dissolved from other factors (e.g., aged dust and the steel industry) because the d-Fe concentrations within the secondary aerosol factor exceeded T-Fe concentrations (Tables S4 and S5). PMF methods were unable to distinguish between direct d-Fe emissions from coal combustion and d-Fe dissolution from aerosol particles acidified by SO_2 emitted from coal combustion due to the covariance of d-Fe concentration with the nss-SO_4^{2-} concentration, a limitation that has also been observed in previous studies (Zhu et al., 2022; Gao et al., 2024; Sun et al., 2024). The contribution of d-Fe to the secondary aerosol factor in this study was higher than those reported for fine aerosol particles collected in urban areas in China as a result of the further chemical alterations of Fe-bearing particles during transport from China to Japan (Zhu et al., 2022; Gao et al., 2024; Sun et al., 2024). Therefore, PMF analysis showed that the aerosol acidification of mineral dust and anthro-Fe plays an important role in the source of d-Fe in fine aerosol particles.

3.5. Monthly variation and size distributions of Fe species

The abundances of Fe species in size-fractionated aerosol particles were estimated through the linear combination fitting of the XANES spectra of aerosol samples with those of reference materials (Fig. S10). Representative Fe species in coarse aerosol particles were ferrihydrite and Fe in crystalline aluminosilicates (e.g., illite, biotite, and smectite; Figs. S10 and S11),

which were similar to the species in mineral dust (Jeong and Achterberg, 2014; Jeong, 2020). The spot analyses of Fe species in coarse aerosol particles revealed that the Fe species in most measurement spots were in accord with those in coarse aerosol particles detected through macroscopic XANES spectroscopy (Fig. S12a). The S intensity of these measurement spots was weak (white circle in Fig. S12d), indicating that fresh mineral dust dominated in the spots. By contrast, Fe(II, III)-sulfates coexisted with aluminosilicate and Fe-(hydr)oxides in spots with high S intensity (green circle in Figs. S12b–S12d). This result indicated that Fe(II, III)-sulfates were present in severely aged mineral dust in coarse aerosol particles. Fe(II, III)-sulfates are water-soluble Fe species that can enhance Fe_{sol}% in aerosol particles. However, their effects on Fe_{sol}% in coarse aerosol particles were not substantial because the abundance of Fe sulfates to that of T-Fe was below the detection limit for macroscopic XANES (Fe-sulfates: T-Fe <10%), in line with the low Fe_{sol}% in coarse aerosol particles.

Fe(II, III)-sulfates and Fe(III)-oxalate were identified to be representative Fe species in fine aerosol particles (Fig. 8a). Fe(III)-oxalate is also known as a water-soluble Fe species. The correlation of the abundance of these water-soluble Fe species with the Fe_{sol}% in fine aerosol particles was the most important result (Fig. 8b). The Fe species in the residue of ultrapure water extraction (i.e., insoluble Fe species) were determined to confirm whether these water-soluble Fe species readily dissolved in water. Crystalline aluminosilicates and Fe oxides (hematite and magnetite) were identified as insoluble Fe species in the residues, whereas Fe(II, III)-sulfates and Fe(III)-oxalate were not detected (Fig. S13). The water-soluble Fe species in fine aerosol particles likely formed through the chemical alterations of insoluble Fe, rather than directly emitted from primary sources. Although Fe(II, III)-sulfates are directly emitted from liquid fuel combustion, PMF analysis did not identify these emissions as the dominant source of Fe in fine aerosol particles. Similarly, Fe(III)-oxalate was not detected in the emission source samples of anthro-Fe. PMF results indicated that the total Fe in fine aerosol particles mainly originated from fresh and aged dust and the steel industry, with the dominant Fe species being primarily aluminosilicates and Fe-oxide nanoparticles. These Fe species were consistent with the insoluble Fe species identified in fine aerosol particles through XAFS spectroscopy. These primary sources, mineral dust, and steel industry–derived anthro-Fe typically exhibit low Fe_{sol}% without atmospheric chemical alterations. However, PMF analysis also revealed that aged dust and steel industry factors had a high Fe_{sol}%, highlighting the importance of the chemical alterations of Fe in mineral dust and anthro-Fe as key processes enhancing the water solubility of Fe in fine aerosol particles.

Aerosol samples in the 0.39–0.69 and 0.69–1.3 μm fractions contained at least one water-soluble Fe species throughout the sampling campaign, whereas the finest fraction did not always contain water-soluble Fe species (Fig. 8a). These results indicated that the degree and process of chemical alterations differed among the finest and 0.39–0.69 and 0.69–1.3 μm fractions. Previous studies have shown that bare Fe-rich particles (uncoated with sulfate and oxalate) were mainly present in particles finer than 0.4 μm; these particles are expected to be minimally aged by atmospheric processes (Zhu et al., 2020; 2022, Xu et al., 2023). By contrast, Fe-rich particles coated with sulfate and oxalate were approximately 0.6 μm in diameter (Zhang et al., 2017; Zhou et al., 2020; Zhu et al., 2020, 2022; Xu et al., 2023). Sulfate and oxalate, mainly formed through chemical reactions in cloud water, were abundant in fine aerosol particles approximately 0.7 ± 0.2 μm in diameter (John et al., 1990;

Meng and Seinfeld, 1994; Yu et al., 2005; Zhang et al., 2017). This diameter was consistent with those of Fe-bearing particles mixed internally with sulfate and oxalate, which are components of cloud interstitial particles with a typical diameter of 0.5–1.0 μm (Zhang et al., 2017; Li et al., 2013; Liu et al., 2018). Therefore, the internal mixing of Fe-bearing particles with SO_4 and oxalate was promoted in cloud water and interstitial cloud particles.

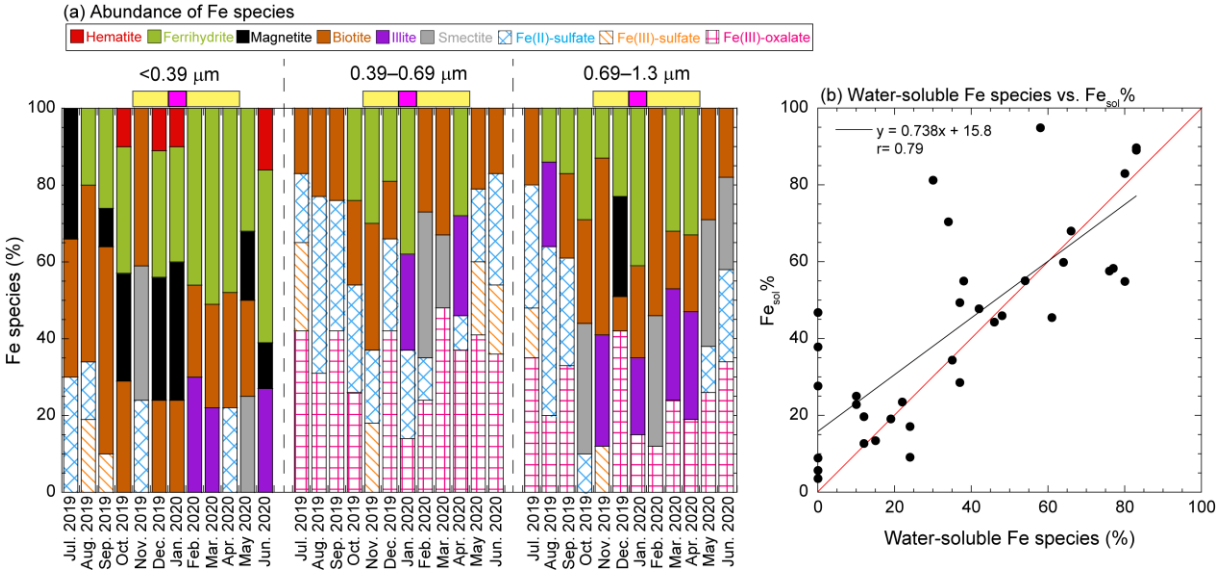

Figure 8. (a) Representative Fe species and their abundances in fine aerosol particles. Water-soluble Fe species (Fe(II)-sulfate, Fe(III)-sulfate, and Fe(III)-oxalate) are shown with lattice patterns. Yellow and pink bars above panels indicate the EAout and COVID-19 lockdown periods, respectively. (b) Scatter plot between the abundances of water-soluble Fe species and Fesol% in fine aerosol particles.

3.6. Alteration processes and dissolution pH of mineral dust

The Fe species in mineral dust and anthropogenic aerosol collected in September 2019 were determined through μ-XRF–XANES to assess the alteration in mineral-Fe and anthro-Fe in fine aerosol particles. μ-XRF–XANES is suitable for the source identification of metal elements in aerosol particles through the determination of elemental compositions and chemical species in regions of interest (Sakata et al., 2017, 2021). In the present study, the regions of interest were Fe-poor spots (M1–M10) and Fe-rich spots (A1–A12, Figs. 9a). The Fe-poor spots contained Ca but lacked anthropogenic metals (e.g., Mn, Ni, Cu, Zn, and Pb, Figs. 9a and S14), indicating that Fe in these spots was associated with mineral dust. M1 spots exhibited low S intensity, and their Fe species were similar to those in mineral dust (aluminosilicates and Fe-(hydr)oxides; Figs. 9a and 9b). These findings were in accord with the μ-XAFS results for coarse aerosol particles. Furthermore, the SEM–EDX of aluminosilicates in coarse aerosol particles collected at the same observation point revealed low amounts of S (Sakata et al., 2021). As mentioned previously, PMF analyses indicated that fresh mineral dust was characterized by the [nss-SO_4^{2-}]/[T-Fe] ratio of 0 (Tables S4 and S5). Therefore, the M1 spots in fine aerosol particles represented fresh mineral dust. By contrast, the XRF

spectra of M2–M10 spots showed an intense S peak, and Fe-containing aluminosilicates were found to coexist with Fe(II, III)-sulfates, suggesting that these Fe-sulfates formed through the chemical alterations of Fe in mineral dust by H_2SO_4. This finding is supported by the PMF analysis, wherein the aged mineral dust factor included nss-SO_4^{2-}. Therefore, the internal mixing of Fe-bearing aluminosilicates with H_2SO_4 is a dominant process for the secondary formation of Fe-sulfates with high Fe_{sol}%. The average abundance of water-soluble Fe species (i.e., Fe(II, III)-sulfates and Fe(III)-oxalate) in M1–M10 was 46% ± 25%, which was higher than that in mineral-Fe_{sol}% (20.3%). This result is partly due to the small number of measurements of Fe species at points of low S intensity, such as the M1 spot.

Given that Fe(III)-oxalate was detected in mineral dust in fine aerosol particles (Fig. 9b), ligand-promoted dissolution appeared to contribute to the dissolution of Fe from mineral dust. Previous research has shown that oxalate plays two key roles in controlling Fe_{sol}% in aerosols depending on their acidity (Myriokefalitakis et al., 2015; Tao and Murphy, 2019; Sakata et al., 2022; Zhang et al., 2024). The first role of oxalate in the dissolution of Fe from mineral dust is to stabilize d-Fe in the aqueous phase in the form of oxalate complexes after proton-promoted dissolution under highly acidic conditions (pH < 3.0). Under such pH conditions, oxalate does not markedly contribute to Fe release from mineral dust because the dissolution rate of Fe from aluminosilicate minerals via proton-promoted dissolution is more than an order of magnitude higher than that via ligand-promoted dissolution (Balland et al., 2010; Cappelli et al., 2020). Additionally, Fe(III)-oxalate can be stabilized in highly acidic solutions (Sakata et al., 2022). This phenomenon not only stabilizes Fe in the aqueous phase but may also promote further Fe dissolution through proton-promoted dissolution by reducing the saturation of inorganic Fe (Ito and Shi, 2016). Therefore, oxalate assists the dissolution of Fe from mineral dust via proton-promoted dissolution under highly acidic conditions. The second role of oxalate is the promotion of Fe dissolution from aluminosilicate under moderately acidic conditions (pH > 3.0). However, ligand-promoted dissolution under moderately acidic conditions cannot dissolve as much Fe from mineral dust as proton-promoted dissolution under highly acidic conditions (Balland et al., 2010). Indeed, previous experiments on the ligand-promoted dissolution of mineral dust in simulated cloud water demonstrated that organic ligands, including oxalates (0–8 μmol L^{-1}), did not achieve a Fe_{sol}% above 10% under moderately acidic conditions (Paris et al., 2011, Paris and Desboeufs, 2013). Therefore, Fe dissolution under highly acidic conditions is necessary to explain high mineral-Fe_{sol}% in fine aerosol particles.

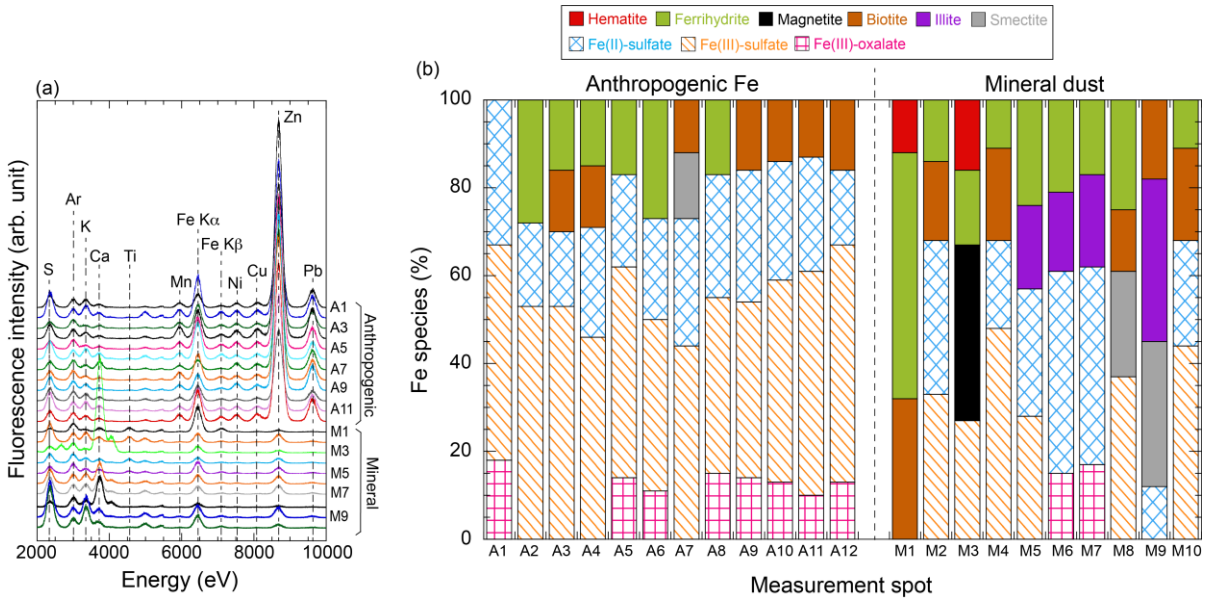

Figure 9. (a) μ-XRF spectra of Fe-rich (anthropogenic: A1–A12) and Fe-poor (mineral: M1–M9) spots in 0.39–0.69 μm aerosol particles collected in September 2019. (b) Abundances of Fe species in each measurement spot.

We estimated the aerosol pH of mineral dust ($pH_{mineral}$) needed to reach the observed mineral-Fe_{sol}% in fine aerosol particles under the assumption that only proton-promoted dissolution occurred to assess whether mineral dust had undergone highly acidic conditions in the atmosphere. The examples for dissolution curve of mineral dust were shown in Figure S15. The average $pH_{mineral}$ during the JPN period (0.60) was lower than that during the EAout period (average $pH_{mineral}$: 1.78; Fig. 10a). The decrease in aerosol pH during summer, as also indicated by aerosol pH estimation using thermodynamic models, can be attributed largely to the enhanced proton activity resulting from high temperatures (Pye et al., 2020; Song and Osada, 2020). Hence, the seasonal variation in $pH_{mineral}$ is likely to be synchronized with the overall changes in aerosol pH. One potential issue is the mitigation of the decrease in the $pH_{mineral}$ of mineral dust in fine aerosol particles due to the buffering capacity of alkaline minerals, including $CaCO_3$. Previous studies have shown that the buffering capacity of alkaline mineral species in fine aerosol particles is almost completely consumed by chemical reactions with H_2SO_4, leading to the formation of $CaSO_4 \cdot 2H_2O$ during transport from East Asia to Japan (Takahashi et al., 2008; Miyamoto et al., 2020). Additionally, the thermodynamic model predicted that the pH of mineral dust would reach 0.0–1.0 after the buffer capacity of $CaCO_3$ is overwhelmed (Meskhidze et al., 2003, 2005). Therefore, the mineral dust in fine aerosol particles can be inferred to have undergone considerable acidification (pH < 2.0). As inferred from these results, Fe(III)-oxalate formed as a result of the stabilization of d-Fe in the aqueous phase following proton-promoted dissolution. This finding was supported by the absence of a correlation between mineral-Fe_{sol}% and the abundance of Fe(III)-oxalate (Fig. 11a). The importance of proton-promoted dissolution for the dissolution of Fe from mineral dust in fine aerosol particles found in our present work was consistent with that observed

in our previous studies because Fe in mineral dust collected above the North Pacific Ocean ([d-Fe]/[d-Al]: 0.26–0.5) dissolved through proton-promoted dissolution under highly acidic conditions, even though organic Fe complexes with humic-like substances are dominant Fe species in fine aerosol particles (Sakata et al., 2022, 2023).

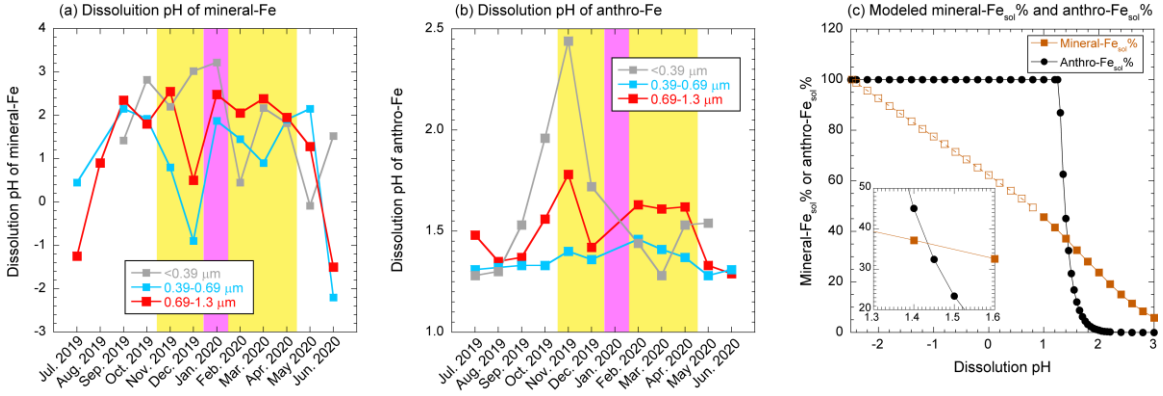

Figure 10. Monthly variations in (a) mineral-Fe_{sol}% and (b) anthro-Fe_{sol}% in fine aerosol particles. Yellow and pink shaded areas show the EAout and COVID-19 lockdown periods, respectively. (c) pH dependences of modeled mineral-$Fe_{sol\%}$ and anthro-Fe_{sol}%. Mineral-Fe_{sol}% plotted with closed symbols was estimated by using the kinetic data shown in Table 1. Mineral-Fe_{sol}% plotted with open symbols was calculated by extrapolating the kinetic equation for pH 1–2 presented in Table 1.

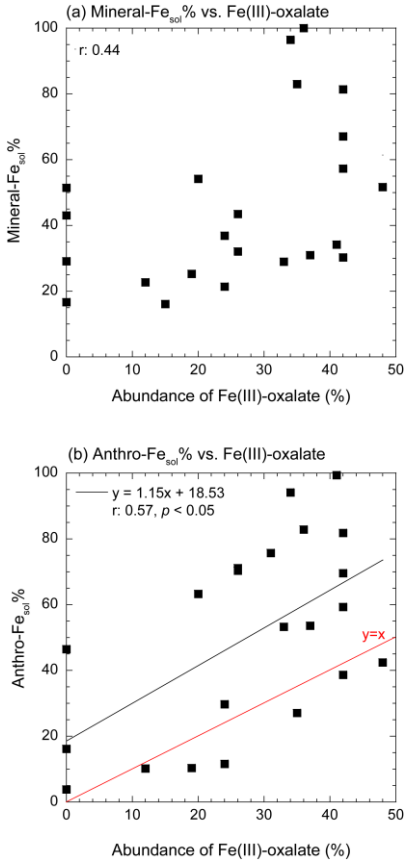

Figure 11. Scatter plots of the abundances of Fe(III)-oxalate with (a) mineral-Fe_{sol}% and (b) anthro-Fe_{sol}% in fine aerosol particles (0.39–0.69 and 0.69–1.3 μm). The black and red lines in panels in (b) show the regression line and y = x, respectively.

3.7. Alteration processes of anthro-Fe

Aerosol particles in Fe-rich spots primarily originated from anthropogenic emissions with high-temperature combustion considering that anthropogenic elements, including Mn, Ni, Cu, Zn, and Pb, were abundant in the spots (A1–A12 in Figs. 9a and S14). Furthermore, Fe intensities in Fe-rich spots were considerably higher than those in Fe-poor spots containing mineral dust. This result suggested that Fe in these spots originated from anthropogenic emissions with high $EF_{T\text{-}Fe}$, including emissions from the steel industry (Tables S4 and S5). A previous study has demonstrated that Fe-rich particles (mainly Fe-oxides) collected directly from steel plants did not contain S but instead acquired a thick sulfate coating over one or two days of transport (Li et al., 2017). Given that the Fe-rich spots exhibited an intense S peak (Fig. 9a), these particles were markedly aged by SO_2 and/or H_2SO_4 in the atmosphere. Consequently, more than half of the Fe in these spots existed in the form of water-soluble Fe species, including Fe(II)-sulfate, Fe(III)-sulfate, and Fe(III)-oxalate (Fig. 9b). The average abundance of water-soluble Fe species in Fe-rich spots (avg ± 1σ: 81% ± 9%) was in agreement with that of anthro-Fe_{sol}% in the sample

estimated by Eq. 4 (74.0%), indicating that the representative anthro-Fe species in this sample can be determined. Furthermore, this consistency supported the reliability of estimating anthro-Fe_{sol}% on the basis of the [d-Fe]/[d-Al] ratio in providing reasonable results.

The number of particles containing Fe(III)-oxalate appeared to be higher in Fe-rich spots than in Fe-poor spots (Fig. 9b). The abundance of Fe(III)-oxalate in fine aerosol particles with diameters of 0.39–0.69 and 0.69–1.3 μm was weakly correlated with anthro-Fe_{sol}% ($r = 0.57$; Fig. 11b). Therefore, oxalate may partially contribute to the dissolution of anthro-Fe. Oxalate in fine aerosol particles formed in cloud water (average pH of East Asia: 4.2, Shah et al., 2020), increasing the number of oxalate-bearing Fe-rich particles through cloud processing (Li et al., 2013; Zhang et al., 2017; Liu et al., 2018). The acquisition of an oxalate coating by anthro-Fe in cloud water promoted Fe dissolution after anthro-Fe was released through cloud water evaporation because the dissolution rate of oxalate-coated hematite at pH 2.4 was higher than that of noncoated hematite (Xu and Gao, 2008). By contrast, proton-promoted dissolution dominated Fe dissolution from hematite under highly acidic conditions ($pH < 2.0$, Xu and Gao, 2008). Under the assumption that anthro-Fe dissolution occurred solely through proton-promoted dissolution, the pH range for the proton-promoted dissolution of anthro-Fe was estimated on the basis of the solubility product of hematite nanoparticles. The predicted pH range for the proton-promoted dissolution of anthro-Fe was narrow (1.3–2.0) due to the sharp increase in anthro-Fe_{sol}% at pH levels below 2.0 (Figs. 10b and 10c). Considering that anthro-Fe had experienced highly acidic conditions and the abundance of Fe(III)-oxalate was lower than that of anthro-Fe_{sol}%, proton-promoted dissolution was inferred to be the primary mechanism for the dissolution of anthro-Fe. Subsequent complexation with oxalate in the aqueous phase to form Fe(III)-oxalate likely reduced the saturation index of inorganic Fe, potentially facilitating further proton-promoted dissolution from the solid phase (Ito and Shi, 2016).

As mentioned previously, anthro-Fe_{sol}% tended to be higher than mineral-Fe_{sol}% for the JPN period, whereas the opposite trend was observed for the EAout period (Figs. S6c–S6e). This difference in seasonal trends can be understood by examining the responsiveness of mineral-Fe and anthro-Fe to the dissolution pH because proton-promoted dissolution was the primary mechanism for mineral-Fe and anthro-Fe. The pH dependence of mineral-Fe_{sol}% and anthro-Fe_{sol}% is illustrated in Fig. 10c. Notably, when the pH was higher than 1.5, mineral-Fe_{sol}% was generally higher than anthro-Fe_{sol}%, whereas anthro-Fe_{sol}% exceeded mineral-Fe_{sol}% at pH levels lower than 1.5 (Fig. 10c). This contrasting behavior occurred because the Fe_{sol}% of hematite nanoparticles, representing anthro-Fe, increased dramatically by approximately three orders of magnitude per unit decrease in pH (Eq. 12), leading to a surge in Fe_{sol}% from roughly 0.1% to 100% as the pH dropped from 2.2 to 1.2. By contrast, mineral-Fe_{sol}% gradually increased with decreasing pH (Fig. 10c). Consequently, anthro-Fe_{sol}% exceeded mineral-Fe_{sol}% within the pH range of 1.4–1.5 (Fig. 10c). In line with this pH-dependent behavior, the pH of samples wherein anthro-Fe_{sol}% exceeded mineral-Fe_{sol}% during the JPN period was considerably lower than 1.4 (average pH: 0.60), whereas that of the samples with high mineral-Fe_{sol}% during the EAout period exceeded 1.4 (average pH: 1.8). Therefore, given that mineral dust and anthro-Fe were emitted in the form of insoluble Fe, the relationship between mineral-Fe_{sol}% and anthro-Fe_{sol}% depended on the pH during reactions (Fig. 10c). This situation implied that the high Fe_{sol}% often seen in fine particles might

not always be linked to anthro-Fe, making determining the origin of aerosol Fe solely on the basis of relative Fe_{sol}% levels difficult.

4. Future implications

In this study, we investigated the factors controlling Fe_{sol}% in size-fractionated aerosol samples collected in the coastal region of the Sea of Japan. Our results showed that the T-Fe and d-Fe concentrations in TSP samples peaked in spring due to the substantial loading of Asian dust into the atmosphere. Steel industry and NEV particles, which were primarily composed of insoluble Fe, were important sources of T-Fe in fine aerosol particles. During the COVID-19 lockdown, the contribution of anthro-Fe (especially from the steel industry) to T-Fe decreased sharply, highlighting that anthro-Fe emitted from combustion and non-combustion sources was a major source of T-Fe in fine aerosol particles over East Asia. Fe_{sol}% was higher in summer than spring, with high values mainly observed in fine aerosol particles, and correlated with the [nss-SO_4^{2-}]/[T-Fe] ratio, indicating that Fe in these fine particles was primarily dissolved through proton-promoted dissolution. Macroscopic and microscopic XANES spectroscopy revealed that the water-soluble Fe species in fine aerosol particles were Fe(II)-sulfate, Fe(III)-sulfate, and Fe(III)-oxalate and were also present in mineral dust and anthropogenic aerosols. Given the water insolubility of Fe species in freshly emitted mineral dust (aluminosilicates) and anthro-Fe (mainly Fe oxides), these water-soluble Fe species likely formed through aerosol acidification by H_2SO_4, a process supported by the strongly acidic conditions suggested by dissolution pH estimations. Therefore, chemical reactions, including aerosol acidification, play a critical role in the control of the Fe_{sol}% of aerosol particles in East Asia.

During the period of increased aerosol outflow from East Asia (November to April), the average Fe_{sol}% of TSPs collected at NOTOGRO (4.9%) was slightly lower than that of TSPs collected in the North Pacific. However, the Fe_{sol}% of fine aerosol particles increased substantially during transportation from East Asia to NOTOGRO, with their average Fe_{sol}% (14.3%) being comparable to that of fine aerosol particles collected in the western Pacific during a similar season (14.2%; Table S3). This finding suggests that the chemical alterations of Fe in mineral dust and anthro-Fe in fine aerosol particles mainly occurred over East Asia rather than during transport in the North Pacific. Therefore, long-term observations on the Fe_{sol}% of the fine aerosol particles collected at the rim of East Asia (i.e., entrance of the North Pacific) play an important role in understanding the controls on Fe_{sol}% supplied to the North Pacific. By contrast, the Fe_{sol}% of coarse aerosol particles were slightly higher in the western Pacific (average: 3.5%) than in NOTOGRO (average: 0.5%). This difference likely contributed to the difference in the Fe_{sol}% of TSPs between the two regions. Therefore, future research should also focus on the Fe dissolution processes in coarse aerosol particles during transport over the marine atmosphere to develop our understanding of aerosol Fe supply to the ocean surface because these differences may be a reason for the higher Fe_{sol}% of TSPs in the western Pacific than in East Asia.

Data Availability.

All quantitative data is approval in ERAN database at https://www.ied.tsukuba.ac.jp/database (doi: 10.34355/CRiES.U.TSUKUBA.00157). The XAFS data are available upon request.

Author Contributions. K.S, S.T., A.M., H.T., and Y.T. designed the research. K.S., A.S., and A.M. collected size-fractionated aerosol samples. S.T determined trace metal concentrations. K.S, Y.T, and M.K. performed macroscopic and micro-focused XAFS experiments. K.S and Y.T. wrote the manuscript, and all authors approved the manuscript before submission.

Competing interests.

The authors declare that they have no conflict of interest.

Acknowledgments

We thank Haruka Naya and Megumi Matsumoto for collecting the aerosol samples. Macroscopic and semi-microscopic XAFS experiments were performed under the approval of the Photon Factory Program Advisory Committee (Proposal No. 2019G093).

Financial support.

This study was supported by Cooperative Research Program of the Institute of Nature and Environmental Technology, Kanazawa University (Proposal No. 19002) and JSPS KAKENHI (Grant Numbers: 20K19957).

Figure captions

Figure 1. Sampling site (NOTOGRO) for size-fractionated aerosols.

Figure 2. Diagram of $EF_{T\text{-}Fe}$ and the [d-Fe]/[d-Al] ratio for evaluating the T-Fe and d-Fe sources of aerosol particles.

Figure 3. (a) Monthly variations in T-Fe concentration and $EF_{T\text{-}Fe}$ in TSPs and (b) size distributions of $EF_{T\text{-}Fe}$ (red line: $EF_{T\text{-}Fe}$ = 2.0). The data of coarse aerosol particles are shown in dashed boxes or lines, whereas those of fine aerosol particles are described in solid boxes or lines. Yellow and pink shaded regions show the EAout and COVID-19 lockdown periods, respectively.

Figure 4. (a) d-Fe concentration and Fe_{sol}% of TSPs; (b) Fe_{sol}%; and (c) the [nss-SO^4_{2-}]/[T-Fe] ratio. The data of coarse aerosol particles are shown in dashed boxes or lines, whereas those of fine aerosol particles are presented in solid boxes or lines. Yellow and pink areas indicate the EAout and COVID-19 lockdown periods, respectively.

Figure 5. (a) Size distribution of the [d-Fe]/[d-Al] ratio. Yellow and pink areas indicate the EAout and COVID-19 lockdown periods, respectively. (b) relationships of $EF_{T\text{-}Fe}$ and the [d-Fe]/[d-Al] ratio. The background color indicates the emission sources of T-Fe and d-Fe, which are detailed in Fig. 2. (c) Correlation between $EF_{T\text{-}Fe}$ and Fe_{sol}%.

Figure 6. Monthly trends of the relative abundances of anthro-Fe to those of (a) d-Fe, (b) mineral-Fe_{sol}%, and (c) anthro-Fe_{sol}% in fine aerosol particles. Yellow and pink shaded regions show the EAout and COVID-19 lockdown periods, respectively. The plots of anthro-Fe_{sol}% in panel (c) are missing because either or both anthro-Fe or anthro-Fe concentrations were 0 due to the remarkable but small contributions of anthro-Fe during the COVID-19 lockdown period.

Figure 7. Panels (a-c) show average contributions to T-Fe, anthro-Fe, and d-Fe, respectively, for the JPN period. Panels (d-f) show contributions to T-Fe, anthro-Fe, and d-Fe, respectively, for the EAout period.

Figure 8. (a) Representative Fe species and their abundances in fine aerosol particles. Water-soluble Fe species (Fe(II)-sulfate, Fe(III)-sulfate, and Fe(III)-oxalate) are shown with lattice patterns. Yellow and pink bars above panels indicate the EAout and COVID-19 lockdown periods, respectively. (b) Scatter plot between the abundances of water-soluble Fe species and Fe_{sol}% in fine aerosol particles.

Figure 9. (a) μ-XRF spectra of Fe-rich (anthropogenic: A1–A12) and Fe-poor (mineral: M1–M9) spots in 0.39–0.69 μm aerosol particles collected in September 2019. (b) Abundances of Fe species in each measurement spot.

Figure 10. Monthly variations in (a) mineral-Fe_{sol}% and (b) anthro-Fe_{sol}% in fine aerosol particles. Yellow and pink shaded areas show the EAout and COVID-19 lockdown periods, respectively. (c) pH dependences of modeled mineral-$Fe_{sol\%}$ and anthro-Fe_{sol}%. Mineral-Fe_{sol}% plotted with closed symbols was estimated by

using the kinetic data shown in Table 1. Mineral-Fe_{sol}% plotted with open symbols was calculated by extrapolating the kinetic equation for pH 1–2 presented in Table 1.

Figure 11. Scatter plots of the abundances of Fe(III)-oxalate with (a) mineral-Fe_{sol}% and (b) anthro-Fe_{sol}% in fine aerosol particles (0.39–0.69 and 0.69–1.3 μm). The black and red lines in panels in (b) show the regression line and y = x, respectively.

References

Balland, C., Poszwa, A., Leyval, C., and Mustin, C.: Dissolution rates of phyllosilicates as a function of bacterial metabolic diversity, Geochim. Cosmochim. Acta, 74, 5478–5493, https://doi.org/10.1016/j.gca.2010.06.022, 2010.

Bibi, I., Singh, B., and Silvester, E.: Dissolution of illite in saline-acidic solutions at 25°C, Geochim. Cosmochim. Ac., 75, 3237–3249, https://doi.org/10.1016/j.gca.2011.03.022, 2011.

Bonneville, S., van Cappellen, P., Behrends, T.: Microbial reduction of iron(III) oxyhydroxides: effects of mineral solubility and availability, Chem. Geol., 212, 255–268, https://doi.org/10.1016/j.chemgeo.2004.08.015, 2004.

Boyd, P. W., Jickells, T., Law, C. S., Blain, S., Boyle, E. A., Buesseler, K. O., Coale, K. H., Cullen, J. J., de Beear, H. J. W., Follows, M., Harvey, M., Lancelot, C., Levasseur, M., Owens, N. P. J., Pollard, R., Rivkin, R. B., Sarmiento, J., Schoemann, V., Smetacek, V., Takeda, S., Tsuda, A., Turner, S., and Watson, A. J.: Mesoscale iron enrichment experiments 1993–2005: Synthesis, and future directions, Science, 315, 612–617, https://doi.org/10.1126/science.1131669, 2007.

Bray, A. W., Oelkers, E. H., Bonneville, S., Wolff-Boenisch, D., Potts, N. J., Fones, G., and Benning, L. G.: The effect of pH, grain size, and organic ligands on biotite weathering rates, Geochim. Cosmochim. Ac., 164, 127–145, https://doi.org/10.1016/j.gca.2015.04.048, 2015.

Buck, C. S., Landing, W. M., and Resing, J.: Pacific Ocean aerosols: Deposition and solubility of iron, aluminum, and other trace elements, Mar. Chem., 157, 117–130, https://doi.org/10.1016/j.marchem.2013.09.005, 2013.

Cappelli, C., Cama, J., van Driessche, A. E. S., and Huertas, F. J.: Biotite reactivity in nitric and oxalic acid at low temperature and acid pH from surface and bulk dissolution measurements, Chem. Geol., 554, 119806, https://doi.org/10.1016/j.chemgeo.2020.119806, 2020.

Chen, C., Huang, L., Shi, J., Zhou, Y., Wang, J., Yao, X., Gao, H., Liu, Y., Xing, J., and Liu, X.: Atmospheric outflow of anthropogenic iron and its deposition to China adjacent seas, Sci. Total Environ., 750, 141302, https://doi.org/10.1016/j.scitotenv.2020.141302, 2021.

Chen, H. and Grassian, V. H.: Iron dissolution of dust source materials during simulated acidic processing: The effect of sulfuric, acetic, and oxalic acids, Environ. Sci. Technol., 47, 10312– 10321, https://doi.org/10.1021/es401285s, 2013.

Falkowski, P., Scholes, R. J., Boyle, E., Canadell, J., Canfield, D., Elser, J., Gruber, N., Hibbard, K., Hogberg, P., Linder, S., Mackenzie, F. T., Moore, B., Pedersen, T., Rosenthal, Y., Seitzinger, S., Smetacek, V., and Steffen, W.: The global carbon cycle: A test of our knowledge of earth as a system, Science, 290, 291–296, https://doi.org/10.1126/science.290.5490.291, 2000.

Fang, T.; Guo, H.; Peltier, R. E., Weber, R. J.: $PM_{2.5}$ water-soluble elements in the southeastern United States: automated analytical method development, spatiotemporal distributions, source apportionment, and implications for heath studies, Atmos. Chem. Phys., 15, 11667–11682, https://doi.org/10.5194/acp-15-11667-2015, 2015

Fu, Z., Wu, Y., Zhao, S., Bai, X., Liu, S., Zhao, H., Hao, Y., Tian, H.; Emissions of multiple metals from vehicular brake linings wear in China, 1980–2020, 889, 164380, https://doi.org/10.1016/j.scitotenv.2023.164380, 2023.

Gao, X., Li, W., Sun, X., Hao, Y., Sun, M., Yang, Y., Wu, G., and Zhou, Y.: The important role of nitrate in iron and manganese dissolution and sulfate formation in fine particles at a coastal site in Northern China, Sci. Total Environ. 921, 170318, https://doi.org/10.1016/j.scitotenv.2024.170318, 2024.

Halle, L. L., Palmqvist, A., Kampmann, K., Jensen, A., Hansen, T., and Khan, F. R.: Tire wear particle and leachate exposures from a pristine and road-worn tire to Hyalella azteca: Comparison of chemical content and biological effects, Aquat. Toxicol., 232, 105769, https://doi.org/10.1016/j.aquatox.2021.105769, 2021.

Hamilton, D. S., Scanza, R. A., Feng, Y., Guinness, J., Kok, J. F., Li, L., Liu, X., Rathod, S. D., Wan, J. S., Wu, M., and Mahowald, N. M.: Improved methodologies for Earth system modelling of atmospheric soluble iron and observation comparisons using the Mechanism of Intermediate complexity for Modelling Iron (MIMI v1.0), Geosci. Model Dev., 12, 3835–3862, https://doi.org/10.5194/gmd-12-3835-2019, 2019.

Hsieh, C. C., Chen, H. Y., and Ho, T. Y.: The effect of aerosol size on Fe solubility and deposition flux: A case study in the East China Sea, Mar. Chem., 241, 104106, https://doi.org/10.1016/j.marchem.2022.104106, 2022.

Ito, A. and Shi, Z.: Delivery of anthropogenic bioavailable iron from mineral dust and combustion aerosols to the ocean, Atmos. Chem. Phys., 16, 85–99, https://doi.org/10.5194/acp-16-85- 2016, 2016.

Ito, A., Ye, Y., Baldo, C., and Shi, Z.: Ocean fertilization by pyrogenic aerosol iron, npj Clim. Atmos. Sci., 4, 30, https://doi.org/10.1038/s41612-021-00185-8, 2021.

Jeong, G. Y., Achterberg, E. P.: Chemistry and mineralogy of clay minerals in Asian and Saharan dusts and the implications for iron supply to the oceans, Atmos. Chem. Phys., 14, 12415–12428, https://doi.org/10.5194/acp-14-12415-2014, 2014.

Jeong, G. Y.: Mineralogy and geochemistry of Asian dust: dependence on migration path, fractionation, and reactions with polluted air, Atmos. Chem. Phys., 20, 7411–7428, https://doi.org/10.5194/acp-20-7411-2020, 2020.

Jickells, T. D., An, Z. S., Andersen, K. K., Baker, A. R., Bergametti, G., Brooks, N., Cao, J. J., Boyd, P. W., Duce, R. A., Hunter, K. A., Kawahata, H., Kubilay, N., laRoche, J., Liss, P. S., Mahowald, N., Prospero, J. M., Ridgwell, A. J., Tegen, I., and Torres, R.: Global iron connections between desert dust, ocean biogeochemistry, and climate, Science, 308, 67–71, https://doi.org/10.1126/science.1105959, 2005.

John, W., Wall, S. M., Ondo, J. L., and Winklmayr, W.: Modes in the size distributions of atmospheric inorganic aerosol, Atmos. Environ., 24A, 2349–2359, https://doi.org/10.1016/0960-1686(90)90327-J, 1990.

Journet, E., Desboeufs, K. V., Caquineau, S., and Colin, J. L.: Mineralogy as a critical factor of dust iron solubility, Geophys. Res. Lett., 35, L07805, https://doi.org/10.1029/2007GL031589, 2008.

Kajino, M., Hagino, H., Fujitani, Y., Morikawa, T., Fukui, T., Onishi, K., Okuda, T., Kajikawa, T., and Igarashi, Y.: Modeling transition metals in East Asia and Japan and its emission sources, GeoHealth, 4, e2020GH00259, https://doi.org/10.1029/2020GH000259, 2020.

Kawai, K., Matsui, H., Tobo, Y.: High potential of Asian dust to act as ice nucleating particles in mixed-phase clouds simulated with a global aerosol-climate model, J. Geophys. Res. Atmos., 126, e2020JD034263, https://doi.org/10.1029/2020JD034263, (2021).

Kurisu, M., Sakata, K., Nishioka, J., Obata, H., Conway, T. M., Hunt, H. R., Sieber, M., Suzuki, K., Kashiwabara, T., Kubo, S., Takada, M., and Takahashi, Y.; Source and fate of atmospheric iron supplied to the subarctic North Pacific traced by stable iron isotope ratios, Geochim. Cosmochim. Acta, 378, 168–185, https://doi.org/10.1016/j.gca.2024.06.009, 2024.

Kurisu, M., Sakata, K., Uematsu, M., Ito, A., and Takahashi, Y.: Contribution of combustion Fe in marine aerosols over the northwestern Pacific estimated by Fe stable isotope ratios, Atmos. Chem. Phys., 21, 16027–16050, https://doi.org/10.5194/acp-21-16027-2021, 2021.

Kurisu, M., Takahashi, Y., Iizuka, T., and Uematsu, M.: Very low isotope ratio of iron in fien aerosols related to its contribution to the surface ocean, J. Geophys. Res.-Atmos., 121, 11119–11136, https://doi.org/10.1002/2016JD024957, 2016.

Kurokawa, J., and Ohara, T.: Long-term historical trends in air pollutant emissions in Asia: Regional emission inventory in Asia (REAS) version 3, Atmos. Chem. Phys., 20, 12761–12793, https://doi.org/10.5194/acp-20-12761-2020, 2020.

Li, R., Zhao, Y., Fu, H., Chen, J., Peng, M., and Wang, C.: Substantial changes in gaseous pollutants and chemical compositions in fine particles in the North China Plain during the COVID-19 lockdown period: anthropogenic vs. meteorological influences, Atmos. Chem. Phys., 21, 8677–8692, https://doi.org/10.5194/acp-21-8677-2021, 2022.

Li, S., Zhang, B., Wu, D., Li, Z., Chu, S. Q., Ding, X., Tang, X., Chen, J., and Li, Q.: Magnetic particles unintentionally emitted from anthropogenic sources: Iron and steel plants, Environ. Sci. Technol., Lett., 8, 295–300, https://doi.org/10.1021/acs.estlett.1c00164, 2021.

Li, W., Wang, Y., Collett Jr., J. L., Chen, J., Zhang, X., Wang, Z., and Wang, W.: Microscopic evaluation of trace metals in cloud droplets in an acid precipitation region, Environ. Sci. Technol., 47, 4172–4180, https://doi.org/10.1021/es304779t, 2013.

Li, W., Xu, L., Liu, X., Zhang, J., Lin, Y., Yao, X., Gao, H., Zhang, D., Chen, J., Wang, W., Harrison, R. M., Zhang, X., Shao, L., Fu, P., Nenes, A., and Shi, Z.: Air pollution-aerosol interactions produce more bioavailable iron for ocean ecosystems, Sci. Adv., 3, e1601749, https://doi.org/10.1126/sciadv.1601749, 2017.

Liu, L., Li, W., Lin, Q., Wang, Y., Zhang, J., Zhu, Y., Yuan, Q., Zhou, S., Zhang, D., Baldo, C., and Shi, Z.: Size-dependent aerosol iron solubility in an urban atmosphere, NPJ Clim. Atmos. Sci., 5, 54, https://doi.org/10.1038/s41612-022-00277-z, 2022.

Liu, L., Lin, Q., Liang, Z., Du, R., Zhang, G., Zhu, Y., Qi, B., Zhou, S., and Li, W.: Variations in concentrations and solubility of iron in atmospheric fine particles during the COVID-19 pandemic: An example from China, Gondwana Res., 97, 138–144, https://doi.org/10.1016/j.gr.2021.05.022, 2021.

Liu, L., Zhang, J., Xu, L., Yuan, Q., Huang, D., Chen, J., Shi, Z., Sun, Y., Fu, P., Wang, Z., Zhang, D., and Li, W.: Cloud scavenging of anthropogenic refractory particles at a mountain site in North China, Atmos. Chem. Phys., 18, 14681–14693, https://doi.org/10.5194/acp-18-14681-2018, 2018.

Liu, X., Turner, J. R., Hand, J. L., Schichtel, B. A., and Martin, R. V.: A global-scale mineral dust equation, J. Geophys. Res.-Atmos., 127, e2022JD036937, https://doi.org/10.1029/2022JD036937, 2022.

Mahowald, N. M., Hamilton, D. S., Mackey, K. R. M., Moore, J. K., Baker, A. R., Scanza, R. A. and Zhang, Y.: Aerosol trace metal leaching and impacts on marine microorganisms, Nat. Commun., 9, 1–15, https://doi.org/10.1038/s41467-018-04970-7, 2018.

Martin, J. H., Coale, K. H., Johnson, K. S., Fitzwater, S. E., Gordon, R. M., Tanner, S. J., Hunter, C. N., Elrod, V. A., Nowicki, J. L., Coley, T. L., Barber, R. T., Lindley, S., Watson, A. J., van Scoy, K., Law, C. S., Liddicoat, M. I., Lng, R., Stanton, T., Stockel, J., Collings, C., Anderson, A., Bidigare, R., Ondrusek, M., Latasa, M., Millero, F. J., Lee, K., Yao, W., Zhang, J. Z. Friederich, G., Sakamoto, C., Chavez, F., Buck, K., Kolber, Z., Greene, R., Falkowski, P., Chisholm, S. W., Hoge, F., Swift, R., Yungel, J., Turner, S., Nightingale, P., Hatton, A., Liss, P., and Tindale, N. W. Testing the iron hypothesis in ecosystems of the equatorial Pacific Ocean, Nature, 371, 123–129, https://doi.org/10.1038/371123a0, 1994.

Martin, J. H.: Glacial-interglacial CO_2 change: The iron hypothesis, Paleoceanogr., 5, 1, 1–13, https://doi.org/10.1029/PA005i001p00001, 1990.

Maters, E. C., Delmelle, P., and Bonneville, S.: Atmospheric processing of volcanic glass: Effects on iron solubility and redox speciation, Environ. Sci. Technol., 50, 5033–5040, https://doi.org/10.1021/acs.est.5b06281, 2016.

Meng, Z., and Seinfeld, J. H.: On the source of submicrometer droplet mode of urban and regional aerosols, Aerosol Sci., Technol., 20, 253–265, https://doi.org/10.1080/02786829408959681, 1994.

Meskhidze, N., Chameides, W. L., and Nenes, A.: Dust and pollution: A recipe for enhanced ocean fertilization?, J. Geophys. Res., 110, D03301, https://doi.org/10.1029/2004JD005082, 2005.

Meskhidze, N., Chameides, W. L., Nenes, A., and Chen, G.: Iron mobilization in mineral dust: can anthropogenic SO_2 emission affect ocean productivity? Geophyes. Res. Lett., 30, GL018035, https://doi.org/10.1029/2003GL018035, 2003.

Miyamoto C., Sakata, K., Yamakawa, Y., and Takahashi, Y.: Determination of calcium and sulfate species in aerosols associated with the conversion of its species through reaction processes in the atmosphere and its influence on cloud condensation nuclei activation, Atmos. Environ., 223, https://doi.org/10.1016/j.atmosenv.2019.117193, 117193, 2020.

Moore, C. M., Mills, M. M., Arrigo, K. R., Berman-Frank, I., Bopp, L., Boyd, P. W., Galbraith, E. D., Geider, R. J., Guieu, C., Jaccard, S. L., Jickells, T. D., La Roche, J., Lenton, T. M., Mahowald, N. M., Marañón, E., Marinov, I., Moore, J. K., Nakatsuka, T., Oschlies, A., Saito, M. A., Thingsted, T. F., Tsuda, A., and Ulloa, O.: Processes and patterns of oceanic nutrient limitation, Nat. Geosci., 6, 701–710, https://doi.org/10.1038/ngeo1765, 2013.

Mori, I., Sun, Z., Ukachi, M., Nagano, K., McLeod, C. Q., Cox, A. G., and Nishikawa, M.: Development and certification of the new NIES CRM 28: urban aerosols for the determination of multielements, Anal. Bioanal. Chem., 391, 1997–2003, https://doi.org/10.1007/s00216-008-2076-y, 2008.

Morton, P. L., Landing, W. M., Hsu, S. C., Milne, A., Aguilar- Islas, A. M., Baker, A. R., Bowie, A. R., Buck, C. S., Gao, Y., Gichuki, S., Hastings, M. G., Hatta, M., Johansen, A. M., Losno, R., Mead, C., Patey, M. D., Swarr, G., Vandermark, A., and Zamora, L. M.: Methods for the sampling and analysis of marine aerosols: Results from the 2008 GEOTRACES aerosol intercalibration experiment, Limnol. Oceanogr. Method., 11, 62– 78, https://doi.org/10.4319/lom.2013.11.62, 2013.

Myriokefalitakis, S., Daskalakis, N., Mihalopoulos, N., Baker, A. R., Nenes, A., Kanakidou, M.: Changes in dissolved iron deposition to the oceans driven by human activity: a 3-D global modelling study, Biogeosci., 12, 3973–3992, https://doi.org/10.5194/bg-12-3973-2015, 2015.

Myriokefalitakis, S., Ito, A., Kanakidou, M., Nenes, A., Krol, M. C., Mahowald, N. M., Scanza, R. A., Hamilton, D. S., Johnson, M. S., Meskhidze, N., Kok, J. F., Guieu, C., Baker, A. R., Jickells, T. D., Sarin, M. M., Bikkina, S., Shelley, R., Bowie, A., Perron, M. M. G., and Duce, R. A.: Reviews and syntheses: The GESAMP atmospheric iron deposition model intercomparison study, Biogeosciences, 15, 6659–6684, https://doi.org/10.5194/bg-15-6659-2018, 2018.

Norris, G., Duvall, R., Brown, S., and Bai, S.: EPA Positive Matrix Factorization (PMF) 5.0 Fundamentals and User Guide, available at: https://www.epa.gov/sites/production/files/2015-02/documents/pmf_5.0_user_guide.pdf (last access: 11 January 2024), 2014.

Oakes, M., Ingall, E. D., Lai, B., Shafer, M. M., Hays, M. D., Liu, Z. G., Russell, A. G., and Weber, R. J.: Iron solubility related to particle sulfur content in source emission and ambient fine particles, Environ. Sci. Technol., 46, 6637–6644, https://doi.org/10.1021/es300701c, 2012.

Paris, R. and Desboeufs, K. V.: Effect of atmospheric organic complexation on iron-bearing dust solubility, Atmos. Chem. Phys., 13, 4895–4905, https://doi.org/10.5194/acp-13- 4895-2013, 2013.

Paris, R., Desboeufs, K. V., Journet, E.: Variability of dust iron solubility in atmospheric waters: Investigation of the role of oxalate organic complexation, Atmos. Environ., 45, 6510–6517, https://doi.org/10.1016/j.atmosenv.2011.08.068, 2011.

Pindado, O., and Perez, R. M.: Source apportionment of particulate organic compounds in rural area of Spain by positive matrix factorization, Atmos. Pollut. Res., 2, 492–505, https://doi.org/10.5094/APR.2011.056, 2011.

Pye, H. O. T., Nenes, A., Alexander, B., Ault, A. P., Barth, M. C., Clegg, S. L., Collett Jr., J. L., Fahey, K. M., Hennigan, C. J., Herrmann, H., Kanakidou, M., Kelly, J. T., Ku, I.-T., McNeill, V. F., Riemer, N., Schaefer, T., Shi, G., Tilgner, A.,Walker, J. T.,Wang, T., Weber, R., Xing, J., Zaveri, R. A., and Zuend, A.: The acidity of atmospheric particles and clouds, Atmos. Chem. Phys., 20, 4809–4888, https://doi.org/10.5194/acp-20-4809-2020, 2020

Rudnick, R. L. and Gao, S.: Composition of the continental crust. Treatise on Geochemistry, 3, 1–64, https://doi.org/10.1016/B0-08-043751-6/03016-4, 2003.

Sakata, K., Kurisu, M., Takeichi, Y., Sakaguchi, A., Tanimoto, H., Tamenori, Y., Matsuki, A., and Takahashi, Y.: Iron (Fe) speciation in size-fractionated aerosol particles in the Pacific Ocean: The role of organic complexation of Fe with humic-like substances in controlling Fe solubility, Atmos. Chem. Phys., 22, 9461–9482, https://doi.org/10.5194/acp-22-9461-2022, 2022.

Sakata, K., Kurisu, M., Tanimoto, H., Sakaguchi, A., Uematsu, M., Miyamoto, C., and Takahashi, Y.: Custommade PTFE filters for ultra-clean size-fractionated aerosol sampling for trace metals, Mar. Chem., 206, 100–108, https://doi.org/10.1016/j.marchem.2018.09.009, 2018.

Sakata, K., Sakaguchi, A., Yamakawa, Y., Miyamoto, C., Kurisu, M., and Takahashi, Y.; Measurement report: Stoichiometry of dissolved iron and aluminum as an indicator of the factors controlling the fractional solubility of aerosol iron – results

of the annual observations of size-fractionated aerosol particles in Japan, Atmos. Chem. Phys., 23, 9815–9836, https://doi.org/10.5194/acp-23-9815-2023, 2023.

Sakata, K., Sakaguchi, A., Yokoyama, Y., Terada, Y., and Takahashi, Y.: Lead speciation studies on coarse and fine aerosol particles by bulk and micro X-ray absorption fine structure spectroscopy, Geochem. J., 51, 215–225, https://doi.org/10.2343/geochemj.2.0456, 2017.

Sakata, K., Takahashi, Y., Takano, S., Matsuki, A., Sakaguchi, A., and Tanimoto, H.: First X-ray spectroscopic observations of atmospheric titanium species: size dependence and the emission source, Environ. Sci. Technol., 55, 10975–10986, https://doi.org/10.1021/acs.est.1c02000, 2021.

Sanderson, P., Su, S. S., Chang, I. T. H., Delgado Saborit, J. M., Kepaptsoglou, D. M., Weber, R. J. M., Harrison, R. M.: Characterisation of iron-rich atmospheric submicrometre particles in the roadside environment, Atmos. Environ., 140, 167–175, http://dx.doi.org/10.1016/j.atmosenv.2016.05.040, 2016.

Schlitzer, R.: Ocean Data View, https://odv.awi.de (last access: 14 June 2025), 2023.

Schroth, A. W., Crusius, J., Sholkovitz, E. R., and Bostick, B. C.: Iron solubility driven by speciation in dust sources to the ocean, Nat. Geosci., 2, 337–340, https://doi.org/10.1038/ngeo501, 2009.

Sedwick, P. N., Sholkovitz, E. R., and Church, T. M.: Impact of anthropogenic combustion emissions on the fractional solubility of aerosol iron: Evidence from the Sargasso Sea, Geochem. Geophys. Geosyst., 8, Q10Q06, https://doi.org/10.1029/2007GC001586, 2007.

Shah, V., Jacob, D. J., Moch, J. M., Wang, X., and Zhai, S.: Global modeling of cloud water acidity, precipitation acidity, and acid inputs to ecosystems, Atmos. Chem. Phys., 20, 12223–12245, https://doi.org/10.5194/acp-20-12223-2020, 2020.

Shi, Z. B., Woodhouse, M. T., Carslaw, K. S., Krom, M. D., Mann, G. W., Baker, A. R., Savov, I., Fones, G. R., Brooks, B., Drake, N., Jickells, T. D., and Benning, L. G.: Minor effect of physical size sorting on iron solubility of transported mineral dust, Atmos. Chem. Phys., 11, 8459–8469, https://doi.org/10.5194/acp-11-8459-2011, 2011b.

Shi, Z., Bonneville, S., Krom, M. D., Carslaw, K. S., Jickells, T. D., Baker, A. R., and Benning, L. G.: Iron dissolution kinetics of mineral dust at low pH during simulated atmospheric processing, Atmos. Chem. Phys., 11, 995–1007, https://doi.org/10.5194/acp-11-995-2011, 2011a.

Shi, Z., Krom, M. D., Bonneville, S., and Benning, L. G.: Atmospheric processing outside clouds increases solubile iron in mineral dust, Environ. Sci. Technol., 49, 1472–1477, https://doi.org/10.1021/es504623x, 2015.

Sholkovitz, E. R., Sedwick, P. N., and Church, T. M.: Influence of anthropogenic combustion emissions on the deposition of soluble aerosol iron to the ocean: Empirical estimates for island sites in the North Atlantic, Geochim. Csmochim. Ac., 73, 14, 3981–4003, https://doi.org/10.1016/j.gca.2009.04.029, 2009.

Sholkovitz, E. R., Sedwick, P. N., Church, T. M., Baker, A. R., and Powell, C. F.: Fractional solubility of aerosol iron: Synthesis of a global-scale data set, Geochim. Cosmochim. Ac., 89, 173–189, https://doi.org/10.1016/j.gca.2012.04.022, 2012.

Shupert, L. A., Ebbs, S. D., Lawrence, J., Gibson, D. J., and Filip, P.: Dissolution of copper and iron from automotive brake pad wear debris enhances growth and accumulation by the invasive macrophyte Salvinia molesta Mitchell, Chemosphere, 92, 45–51, https://doi.org/10.1016/j.chemosphere.2013.03.002, 2013.

Song, Q., and Osada, K.: Seasonal variation of aerosol acidity in Nagoya, Japan and factors affecting it, Atmos. Environ., 5, 200062, https://doi.org/10.1016/j.aeaoa.2020.100062, 2020.

Spokes, L., Jickells, T. D., and Lim, B.: Solubilisation of aerosol trace metals by cloud processing: A laboratory study, Geochim. Cosmochim. Ac., 58, 3281–3287, https://doi.org/10.1016/0016- 7037(94)90056-6, 1994.

Sun, M., Qi, Y., Li, W., Zhu, W., Yang, Y., Wu, G., Zhang, Y., Zhao, Y., Shi, J., Sheng, L., Wang, W., Liu, Y., Qu, W., Wang, X., and Zhou, Y.: Investigation of a haze-to-dust and dust swing process at a coastal city in northern China part II: A study on the solubility of iron and manganese across aerosol sources and secondary processes, Atmos. Environ., 328, 120532, https://doi.org/10.1016/j.atmosenv.2024.120532, 2024.

Takahashi, Y., Furukawa, T., Kanai, Y., Uematsu, M., Zheng, G., and Marcus, M. A.: Seasonal changes in Fe species and soluble Fe concentration in the atmosphere in the Northwest Pacific region based on the analysis of aerosols collected in Tsukuba, Japan, Atmos. Chem. Phys., 13, 7695–7710, https://doi.org/10.5194/acp-13-7695-2013, 2013.

Takahashi, Y., Miyoshi, T., Yabuki, S., Inada, Y., and Shimizu, H.: Observation of transformation of calcite to gypsum in mineral aerosols by Ca K-edge X-ray absorption near-edge structure (XANES), Atmos. Environ., 42, 6536–6541, https://doi.org/10.1016/j.atmosenv.2008.04.012, 2008.

Tao, Y. and Murphy, J. G.: The mechanisms responsible for the interactions among oxalate, pH, and Fe dissolution in $PM_{2.5}$, ACS Earth Space Chem., 3, 2259–2265, https://doi.org/10.1021/acsearthspacechem.9b00172, 2019.

Taylor, S. R. and McLennan, S. M.: The geochemical evolution of the continental crust. Rev. Geophys., 33, 241–265, https://doi.org/10.1029/95RG00262, 1995.

Taylor, S. R.: Abundance of chemical elements in the continental crust: a new table, Geochim. Cosmochim. Acta, 28, 1273–1285, https://doi.org/10.1016/0016-7037(64)90129-2, 1964.

Turekian, K. K. and Wedepohl, K. H.: Distribution of the elements in some major units of the Earth's crust. Geol. Soc. Am. Bullet., 72, 175–192, https://doi.org/10.1016/0016-7037(64)90129-2, 1961.

Ueda, S., Iwamoto, Y., Taketani, F., Liu, M., and Matsui, H: Morphological features and water solubility of iron in aged fine aerosol particles over the Indian Ocean, Atmos. Chem. Phys., 23, 10117–10135, https://doi.org/10.5194/acp-23-10117-2023, 2023.

Uematsu, M., Duce, R. A., Prospero, J. M., Chen, L., Merrill, J. T., and McDonald, R. L.: Transport of mineral aerosol from Asia over the North Pacific ocean, J. Geophys. Res., 88, 5342–5352, https://doi.org/10.1029/jc088ic09p05343, 1983.

Wang, S. X., Zhao, B., Cai, S. Y., Klimont, Z., Nielsen, C. P., Morikawa, T., Woo, J. H., Kim, Y., Fu, X., Xu, J. Y., Hao, J. M., and He, K. B.: Emission trends and mitigation options for air pollutants in East Asia, Atmos. Chem. Phys., 14, 6571–6603, https://doi.org/10.5194/acp-14-6571-2014, 2014.

Wedepohl, K. H.: The composition of the continental crust. Geochim. Cosmochim. Acta, 59, 1217– 1232, https://doi.org/10.1016/0016-7037(95)00038-2, 1995.

Wong, J. P. S., Yang, Y., Fang, T., Mulholland, J. A., Russell, A. G., Ebelt, S., Nenes, A., Weber, R. J.; Fine particle iron in soils and road dust is modulated by coal-fired power plant sulfur, Environ. Sci. Technol., 54, 7088–7096, https://dx.doi.org/10.1021/acs.est.0c00483, 2020.

Xu, H., Chen, L., Chen, J., Bao, Z., Wang, C., Gao, X., and Cen, K.: Unexpected rise of atmospheric secondary aerosols from biomass burning during the COVID-19 lockdown period in Hangzhou, China, Atmos. Environ., 278, 119076, https://doi.org/10.1016/j.atmosenv.2022.119076, 2022.

Xu, L., Zhi, M., Liu, X., Gao, H., Yao, X., Yuan, Q., Fu, P., and Li, W.: Direct evidence of pyrogenic aerosol iron by intrusions of continental polluted air into the Eastern China Seas, Atmos. Res., 292, 106839, https://doi.org/10.1016/j.atmosres.2023.106839, 2023.

Xu, N, and Gao, Y.: Characterization of hematite dissolution affected by oxalate coating, kinetics, and pH, Appl. Geochem., 23, 783–793, https://doi.org/10.1016/j.apgeochem.2007.12.026, 2008.

Yu, J. Z., Huang, X. F., Xu, J., and Hu, M.: When aerosol sulfate goes up, so dose oxalate: Implication for the formation mechanisms of oxalate, Environ. Sci. Technol., 39, 128–133, https://doi.org/10.1021/es049559f, 2005.

Zhang, G., Lin, Q., Peng, L., Yang, Y. , Fu, Y., Bi, X., Li, M., Chen, D., Chen, J., Cai, Z., Wang, X., Peng, P., Sheng, G., Zhou, Z.: Insight into the in-cloud formation of oxalate based on in situ measurement by single particle mass spectrometry, Atmos. Chem. Phys., 17, 13891–13901, https://doi.org/10.5194/acp-17-13891-2017, 2017.

Zhang, G., Lin, Q., Peng, L., Yang, Y., Jiang, F., Liu, F., Song, W., Chen, D., Cai, Z., Bi, X. Miller, M., Tang, M., Huang, W., Wang, X., Peng, P. and Sheng, G.: Oxalate formation enhanced by Fe-containing particles and environmental implications, Environ. Sci. Technol., 53, 1269–1277, https://doi.org/10.1021/acs.est.8b05280, 2019.

Zhang, Z., Tao, J., Zhang, L., Hu, B., Liu, M., Nie, F., Lu, H., Chen, L., Wu, Y., Chen, D., Wang, B., and Che, H.: Influence of sources and atmospheric processes on metal solubility in $PM_{2.5}$ in urban Guangzhou, South China, Sci. Total Environ., 951, 175807, https://doi.org/10.1016/j.scitotenv.2024.175807, 2024.

Zheng, H., Kong, S., Chen, N., Yan, Y., Liu, D., Zhu, B., Xu, K., Cao, W., Ding, Q., Lan, B., Zhang, Z. Zheng, M., Fan, Z., Cheng, Y., Zheng, S., Yao, L., Bai, Y., Zhao, T., and Qi, S.: Significant changes in the chemical compositions and sources of PM2.5 in Wuhan since the city lockdown as COVID-19, Sci. Total Environ., 739, https://doi.org/10.1016/j.scitotenv.2020.140000, 140000, 2020.

Zhou, Y., Zhang, Y, Griffith, S. M., Wu, G., Li, L., Zhao, Y., Li, M., Zhou, Z., and Yu, J. Z.: Field evidence of Fe-mediated photochemical degradation of oxalate and subsequent sulfate formation observed by single particle mass spectrometry, Environ. Sci. Technol., 54, 6562–6574, https://doi.org/10.1021/acs.est.0c00443, 2020.

Zhu, Q., Liu, Y., Shao, T., Tang, Y.: Transport of Asian aerosols to the Pacific Ocean, Atmos. Res., 234, 104735, https://doi.org/10.1016/j.atmosres.2019.104735, 2020.

Zhu, Y., Li, W., Lin, Q., Yuan, Q., Liu, L., Zhang, J., Zhang, Y., Shao, L., Niu, H., Yang, S., and Shi, Z.: Iron solubility in fine particles associated with secondary acidic aerosols in east China, Environ. Pollut., 264, 114769, https://doi.org/10.1016/j.envpol.2020.114769, 2020.

Zhu, Y., Li, W., Wang, Y., Zhang, J., Liu, L., Xu, L., Xu, J., Shi, J., Shao, L., Fu, P., Zhang, D., and Shi, Z.: Sources and processes of iron aerosols in a megacity in Eastern China, Atmos. Chem. Phys., 22, 2191–2202, https://doi.org/10.5194/acp- 22-2191-2022, 2022.